Self-lofting of wildfire smoke in the troposphere and stratosphere caused by radiative heating: simulations vs space lidar observations

Kevin Ohneiser[1], Albert Ansmann[1], Jonas Witthuhn[1], Hartwig Deneke[1], Alexandra Chudnovsky[2], and Gregor Walter[1]

[1]Leibniz Institute for Tropospheric Research, Leipzig, Germany
[2]Tel Aviv University, Porter School of Earth Sciences and Environment, Tel Aviv, Israel

Correspondence: K. Ohneiser
(ohneiser@tropos.de)

Abstract. Wildfire smoke is known as a highly absorptive aerosol type in the shortwave wavelength range. The absorption of Sun light by optically thick smoke layers results in heating of the ambient air. This heating is translated into self-lofting of the smoke up to more than 1 km in altitude per day. This study aims for a detailed analysis of tropospheric and stratospheric smoke lofting rate simulations as well as comparisons between modeled and observed smoke lofting rates. One of the main goals is to demonstrate that self-lofting processes can explain observed smoke lofting in the free middle and upper troposphere up to the tropopause and into the lower stratosphere without the need for pyrocumulonimbus convection. Simulations are conducted by using the ECRAD (European Centre for Medium-Range Weather Forecasts Radiation) scheme. As input parameters thermodynamic profiles from CAMS (Copernicus Atmosphere Monitoring Service) reanalysis data, aerosol profiles from ground-based lidar observations, radiosonde potential temperature profiles, CALIOP (Cloud Aerosol Lidar with Orthogonal Polarization) aerosol measurements, and MODIS (Moderate Resolution Imaging Spectroradiometer) aerosol optical depth retrievals were used. The uncertainty analysis revealed that the lofting rate sensitively depends on the aerosol optical thickness (AOT), layer thickness, layer height, and the black carbon to organic carbon fraction. We also looked at the influence of different meteorological parameters such as cloudiness, relative humidity, and potential temperature gradient. Largest sensitivities between 30% and 50% were found for variation of AOT, black carbon fraction, and cloudiness. Uncertainty in the self-lofting estimations grows with longevity of the smoke layers. In recent years, several major wildfire events occurred and injected smoke into the upper troposphere and lower stratosphere. Self-lofting processes led to the ascend of these smoke plumes. CALIPSO measurements show that in 2017, Canadian wildfire smoke plumes ascended by about 10 km in one month. In 2020, Australian wildfire smoke layers were lofted by around 20 km in two months. In 2019 and 2021, significant self-lofting of tropospheric smoke was observed in Siberia. Smoke was injected to around 4 km height and reached the tropopause within less than a week. These four examples, observed with CALIOP, are presented in this study. The observed CALIOP ascent rates are compared to the calculated ascent rates using the ECRAD model heating rate simulations.

1   Introduction

Uncontrolled intense fires on extremely large areas have become more frequently in recent years in many regions on Earth (Jolly et al., 2015; Peterson et al., 2021). Enormous amounts of biomass-burning smoke were emitted into the atmosphere by fire storms in Canada 2017 (Peterson et al., 2018) and Australia 2019-2020 (Peterson et al., 2021). When reaching the stratosphere, wildfire smoke can sensitively influence the stratospheric composition on a hemispheric scale (Bond et al., 2013; Baars et al., 2019; Kloss et al., 2019; Yu et al., 2019; Rieger et al., 2021; Ohneiser et al., 2022) and thus can affect the Earth's climate (Das et al., 2021; Yu et al., 2021; Hirsch and Koren, 2021; Stocker et al., 2021; Heinold et al., 2021; Rieger et al., 2021) and the ozone layer (Ohneiser et al., 2021, 2022; Voosen, 2021; Yu et al., 2021; Rieger et al., 2021; Stone et al., 2021; Solomon et al., 2022; Ansmann et al., 2022). One typical way of biomass-burning smoke plumes to reach the stratosphere is via pyrocumulonimbus (pyroCb) convection (Fromm and Servranckx, 2003; Fromm et al., 2010; Peterson et al., 2018; Rodriguez et al., 2020). These fire-generated clouds can loft large smoke amounts to the tropopause level in less than an hour (Rosenfeld et al., 2007; Rodriguez et al., 2020). From here, smoke is able to ascend deeply into the lower stratosphere by so-called self-lofting processes. Khaykin et al. (2020), Ohneiser et al. (2020, 2022), Kablick et al. (2020), and Hirsch and Koren (2021) analyzed extended smoke layers, originating from the record-breaking Australian wildfires in December 2019 and January 2020, that ascended from 14 to more than 30 km height within 2 months between January 2020 and March 2020 as a result of self-lofting processes.

Figure 1 provides a first impression of the relevance of self-lofting on observable smoke layering features. MODIS satellite observations of smoke plumes that travel from Australia to New Zealand in January 2020 are shown. The brown colors, partly above white cloud layers (see yellow arrows in Fig. 1), indicate extended wildfire smoke fields in the upper troposphere and lower stratosphere (UTLS). The inhomogeneous structures in the smoke layers reflect differences in the smoke aerosol optical thickness (AOT). Plume segments with high AOT above white cloud fields absorb much more sunlight and ascend much faster and higher than smoke plumes with lower AOT over cloud-free areas. As a consequence, originally compact layers with a vertical extent of, e.g., 2 km close to Australia may develop diffusive smoke structures caused by different ascent rates during long-range transport and may show up as 4-8 km deep layers at much higher altitudes after the journey of 10000 km as observed over Punta Arenas in southern Chile in January 2020 (Ohneiser et al., 2022). The dependence of smoke lofting on AOT, meteorological conditions, black carbon fraction, injection height and further relevant quantities will be discussed in Sect. 3.

Recently, smoke self-lofting was observed in the middle and upper troposphere as well (Ohneiser et al., 2021; Engelmann et al., 2021). Large fires in Siberia in July and August 2019 caused a high smoke AOT of 1-2.5 over an area north and northeast of Lake Baikal of more than 500-1000 km for several weeks and triggered the ascent of large amounts of smoke towards the tropopause (Ohneiser et al., 2021). The smoke ascended slowly (compared to fast pyroCb lofting) and reached the tropopause level after several days of continuous lofting. Siberian smoke layers were observed in the stratosphere over Central Europe in August 2019 (Ansmann et al., 2021a) as well as over the High Arctic throughout the entire winter half year (Ohneiser et al., 2021). In 2021, again large and dense plumes of biomass-burning smoke filled the entire troposphere over the fire places in

Siberia in the absence of pyroCb convection as spaceborne lidar observations indicated (CALIPSO, 2022). Part of the smoke again entered the stratosphere in August 2021.

Wildfire smoke is a highly absorptive aerosol type mostly consisting of organic carbon (OC) with a few percent of black carbon (BC). By absorbing solar radiation, optically thick smoke layers are able to considerably heat the ambient air. This
60   heating creates buoyancy which causes the warmed layers to ascend (Boers et al., 2010; de Laat et al., 2012; Yu et al., 2019; Torres et al., 2020). The self-lofting process can prevail for several weeks to months (Kablick et al., 2020; Khaykin et al., 2020; Allen et al., 2020; Lestrelin et al., 2021). The importance of self-lofting is that wildfire smoke can reach high altitudes in this way and can be efficiently distributed over large parts of the hemisphere (Baars et al., 2019; Kloss et al., 2019; Rieger et al., 2021) and a large height range of 10-15 km (Ohneiser et al., 2022). This lofting process leads to a prolongation of the residence
65   time of aerosols in the stratosphere and counteracts the sedimentation and removal of particles.

Not only smoke layers are able to ascend. A similar lofting behavior was observed during the first few days after volcanic eruptions (Muser et al., 2020; Stenchikov et al., 2021) caused by dense light-absorbing ash plumes. Even layers of mineral dust particles were found to ascend by self-lofting (Daerden et al., 2015; Gasteiger et al., 2017). In the spring and summer seasons during the Iraq War (2003-2010) extended plumes of mineral dust due to military activites (mixed with black smoke) were
70   observed, covering large areas over Iraq and adjacent countries (Chudnovsky and Kostinski, 2020). The observed polluted dust features may have been partly influenced by self-lofting effects prolonging residence times and dispersion of pollution and dust over larger areas especially during the summer half years. However, for pure desert dust layers the self-lofting process may be less efficient due to the high weight of the particles and its lower absorption efficiency. In the case of volcanic ash, signifcant lofting was found during the first 3-4 days after the injection of dense ash plumes into the lower stratosphere only (Stenchikov
75   et al., 2021). In contrast, smoke layers were observed to ascend even after two months of injection (Khaykin et al., 2020).

The potential of stratospheric smoke self-lofting processes have already been highlighted in a number of articles, however, a detailed analysis covering even the troposphere has not been presented. Furthermore, the potential and limits of self-lofting simulations including an extended analysis of the impact of uncertainties in the numerous input parameters has not been discussed in sufficient detail. Such an effort is presented in this article for both tropospheric as well as stratospheric smoke
80   plumes and layers. Besides the error analysis, we will apply the developed self-lofting simulation tool to several cases of ascending smoke layers as observed with the space lidar CALIOP (Cloud Aerosol Lidar with Orthogonal Polarization) of the CALIPSO (Cloud-Aerosol Lidar and Infrared Pathfinder Satellite Observations) mission (Winker et al., 2009). These comparisons of simulations with observations allow us to adjust important input parameters such as the BC fraction and to obtain an improved insight into the chemical composition and microphysical properties of wildfire smoke particles.

85   The paper is organized as follows. In Sect. 2, the modeling tools applied to simulate the self-lofting processes are introduced. Section 3 presents an uncertainty discussion with focus on the influence of BC/OC fraction, plume height and geometrical layer depth, and aerosol plume optical thickness on the smoke lofting rates. In Sect. 4, CALIOP observations of different ascending tropospheric and stratospheric smoke plumes obver Canada (2017), Australia (2019-2020), and Siberia (2019, 2021) are compared with respective model simulations. A brief summary and concluding remarks are given in Sect. 5.

2 Radiative Transfer and Lofting Rate Calculations

Biomass-burning smoke particles are assumed in many atmospheric applications to consist of a BC-containing core that is coated with OC substances (Ansmann et al., 2021b). Dahlkötter et al. (2014) found a typical BC core diameter of 130 nm with a mean coating thickness of 105-136 nm in wildfire smoke layers at 10 km height after long-range transport from North America towards Central Europe. Yu et al. (2021) and also Torres et al. (2020) assumed that the aged wildfire smoke plumes in the stratosphere contain a BC fraction of around 2.5%. Such a small fraction of BC is the main driver for a strong persistent radiative heating of the smoke layers. The resulting ascent rate, however, depends in a complex way on the vertical gradient of the potential temperature, BC/OC fraction, plume height and depth as well as plume aerosol optical thickness (Boers et al., 2010; de Laat et al., 2012). Significant differences in the tropospheric and stratospheric lofting characteristics exist (Ohneiser et al., 2020, 2021).

The calculation scheme for the self-lofting rate of a smoke layer consists of two independent steps. First, the radiative heating caused by smoke absorption of solar radiation is determined based on radiative transfer calculations. Second, the heating rate is converted to a lofting rate considering the atmospheric profile of potential temperature following Boers et al. (2010). Figure 2 provides an overview of the self-lofting rate calculation scheme. We will explain the scheme in Sect. 2.1-2.4. At TROPOS, several efforts have been conducted to quantify the radiative effects of clouds and aerosols (e.g. Hanschmann et al. (2012); Kanitz et al. (2013); Barlakas et al. (2020); Witthuhn et al. (2021); Barrientos-Velasco et al. (2022)). This has lead to the development of a Python-based utility library called the TROPOS Cloud and Aerosol Radiative Effects simulator (TCARS). This library has been applied in our study together with the ECRAD radiative transfer scheme (ECWMF Radiation scheme, Hogan and Bozzo (2018); ECRAD (2022)) to determine the radiative heating rate caused by the absorbing smoke aerosol layers. ECRAD generally allows for 3D calculations of radiative transfer in cloudy and cloud-less aerosol-polluted atmospheres (Hogan and Bozzo, 2018). The 3D calculations were, however, not used here. The key input parameter of interest for our purpose is the vertical profile of the aerosol mass mixing ratio or the particle extinction coefficient (see Fig. 2).

2.1 Aerosol profiles as input

Figure 3a shows an example of particle backscatter and extinction profiles at 532 nm as measured with ground-based lidar at Punta Arenas, Chile, in January 2020 (Ohneiser et al., 2022). Australian fire smoke reached heights of 19-23 km by self-lofting during the long-range transport from Australia to South America. The extinction profile is obtained by multiplying the backscatter coefficient with an extinction-to-backscatter ratio (lidar ratio) of 91 sr. This high lidar ratio is indicative for strongly absorbing smoke particles (Ohneiser et al., 2020, 2022).

For the ECRAD model input, Gaussian-shaped profiles in Fig. 3b were then used as input. The green curve is scaled to the same AOT of 0.18 as well as same layer height and layer thickness as observed. The blue curve is scaled to an AOT of 0.22, and the olive profile to an AOT of 0.1. Layer center height and thickness were varied in the different simulation scenarios.

ECRAD requires mass mixing ratio profiles (see Fig. 2). Therefore, the extinction coefficient α was converted to the mass mixing ratio $m = \alpha c_{\mathrm{v}} \rho_{\mathrm{aer}} / \rho_{\mathrm{air}}$. The volume-to-extinction conversion factor $c_{\mathrm{v}} = 0.13 \cdot 10^{-12}\,\mathrm{Mm}^{-1}$ is taken from Ansmann et al. (2021b) for aged smoke far away from fire regions. For the smoke particle density ρ_{aer} we assumed a value of $1.15\,\mathrm{g\,cm}^{-3}$

125 (Ansmann et al., 2021b). The air density ρ_{air} is calculated from CAMS (Copernicus Atmosphere Monitoring Service) meteorological reanalysis data (CAMS, 2022). The aerosol was then handled as an external mixture of organic carbon particles and black carbon particles with adjustable concentrations. It is known that black carbon can exist in one of several possible mixing states (Jacobson, 2001). The assumption on the selected mixing state of the smoke particles in the simulations is further discussed in Sect. 2.4.

130 ## 2.2 Heating rate calculation

With the aerosol profiles in Fig. 3, aerosol optical parametrization settings in Fig. 4, given Sun position, and the CAMS reanalysis meteorological data file, ECRAD calculates the upwelling '↑' and downwelling '↓' shortwave 'short' and longwave 'long' radiation $F_{\uparrow,\mathrm{short}}$, $F_{\downarrow,\mathrm{long}}$, $F_{\uparrow,\mathrm{long}}$, and $F_{\downarrow,\mathrm{short}}$, respectively, at each pre-defined height and pressure level (see Fig. 2). Simulations were conducted for 991 pressure bins between the surface and $40\,\mathrm{km}$ height. The resulting radiation information is

135 translated into radiative heating information. The radiative flux divergence, meaning the differential change of radiative flux at the top or bottom of a layer defines the radiative heating of the layer. The change of temperature $\mathrm{d}T$ with time $\mathrm{d}t$ is defined by the gravitational acceleration g_{E}, the specific heat of air c_p, and the net change of radiation $\mathrm{d}F_{\mathrm{tot}}$ between two pressure levels $\mathrm{d}p$ with $\mathrm{d}T/\mathrm{d}t = g_{\mathrm{E}}/c_{\mathrm{p}}(\mathrm{d}F_{\mathrm{tot}}/\mathrm{d}p)$ from Hicke et al. (1999) with $\mathrm{d}F_{\mathrm{tot}} = \mathrm{d}F_{\mathrm{short}} + \mathrm{d}F_{\mathrm{long}} = \mathrm{d}F_{\uparrow,\mathrm{short}} - \mathrm{d}F_{\downarrow,\mathrm{short}} + \mathrm{d}F_{\uparrow,\mathrm{long}} - \mathrm{d}F_{\downarrow,\mathrm{long}}$.

In order to get a daily-average heating rate in $\mathrm{K\,day}^{-1}$, the radiative heating calculations take a Sun position parametrization

140 into account in terms of time, geographical coordinates, and season (see Fig. 2). To avoid a very detailed consideration of the diurnal cycle of the Sun, we computed the heating and lofting rates every three hours between 0 and 21 UTC and used the mean value of the eight calculations as the representative heating and lofting rate for this specific day. The daily-average heating rate is calculated inside the pre-defined aerosol layer.

2.3 Lofting rate calculations

145 In the last step of the calculation of the lofting rate $\mathrm{d}z$ (see Fig. 2, red part), the heating rate from Sect. 2.2 (now $\mathrm{d}\Theta = \mathrm{d}T/\mathrm{d}t$) is divided by the potential temperature gradient Γ as in Eq. 3 in Boers et al. (2010) rewritten as $\mathrm{d}z = \mathrm{d}\Theta/\Gamma$. Figure 5 shows height profiles of the potential temperature gradient Γ at Punta Arenas (-53.17°N, -70.93°E, Chile) for January 2020, Olenek (68.50°N, 112.43°E, Russia) for July-August 2019, and Port Hardy (50.68°N, -127.36°E, USA) for August 2017. In this post-processing step, the CAMS data is not used. Instead, the radiosonde atmospheric data shown in Fig. 5 is applied (Uni-Wyoming, 2022). As

150 the potential temperature gradient is strongly influencing the ascent rate, the local radiosonde data is chosen as the most precise data for this application. These profiles were individually applied to the final lofting rate calculations in the respective regions. The profiles look very similar to each other with potential temperature gradients around $5\,\mathrm{K\,km}^{-1}$ in the troposphere, a strong gradient of the potential temperature gradient at the tropopause and a steadily increasing gradient within the stratosphere up to

$40 \, \mathrm{K \, km^{-1}}$ at $30 \, \mathrm{km}$ height. Only the height of the tropopause differs between the three locations with around $10 \, \mathrm{km}$ at Punta

155 Arenas and around $12 \, \mathrm{km}$ at Port Hardy.

2.4 Optical properties of Smoke Particles

The variety of optical properties of different fire smoke mixtures, and as a consequence, the number of parametrizations used in simulations is large. In this study, an external mixture of black carbon and brown carbon with adjustable black carbon fraction is priorized instead of an aggregate consisting of both aerosol types. Jacobson (2001) found that an external mixture of black

160 carbon and other aerosol types potentially leads to an underestimation of radiative forcing compared to an internal mixture. Shiraiwa et al. (2008) estimated that internal mixing enhances the BC absorption by a factor of 1.5–1.6 compared to external mixing. For smaller BC cores (or fractal agglomerates) consideration of the BC and brown carbon as an external mixture leads to relatively small errors in the particle single scatter albedo of <0.03 (Lack and Cappa, 2010). Lesins et al. (2002) found, however, that the difference in extinction, single scattering albedo, and asymmetry parameter, between an internal mixture and

165 external mixture of black carbon and ammonium sulfate can be >25% for the dry case and >50% for the wet case for typical mass mixing ratios. Liu and Mishchenko (2007), on the other hand, show that the optical cross-sections of externally mixed aggregates is up to 20% larger than of multi-component aggregates. Typically, the organic carbon fraction was set around 97.5% and the black carbon fraction around 2.5% (Yu et al., 2019, 2021; Torres et al., 2020). More work on the relationship between smoke chemical and microphyscial properties and resulting optical properties is required.

170 The optical properties in terms of single scattering albedo SSA and asymmetry factor g of the hydrophobic organic matter as well as three different black carbon parametrizations are summarized in Fig. 4. SSA describes the ratio of scattering efficiency to total extinction efficiency and g describes the mean cosine of the scattering angle when integrating over the complete scattering phase function. The organic carbon parametrization (OPAC: Optical Properties of Aerosols and Clouds) (Hess et al., 1998) shows a high single scattering albedo as well as high asymmetry factors at all wavelengths between $200 \, \mathrm{nm}$

175 and $3400 \, \mathrm{nm}$ compared to the three different shown black carbon parametrizations. Even though the aerosol mixture usually consists of only $\approx$3% BC aerosol, the low BC SSA and g values widely determine the total absorbing characteristics. Three BC parametrizations are shown for comparison in Fig. 4. Parametrization 1: OPAC (Hess et al., 1998), parametrization 2: Bond and Bergstrom (2006), parametrization 3: Stier et al. (2007). All the three parametrizations are quite similar regarding their optical properties, however, parametrization 1 shows a slightly enhanced asymmetry factor. In the following calculations all

180 parametrizations are used, however, if not stated differently in the text, the OPAC parametrization is applied.

3 Sensitivity of self-lofting rate simulations

The following section focuses on the simulations of lofting rates for different smoke plume characteristics and aerosol scenarios in the troposphere and stratosphere. Different BC parametrizations and BC/OC fractions, AOT, and layer thicknesses are considered. Furthermore, the influence of different atmospheric background situations regarding cloudiness or relative humidity

185 on the lofting rate is investigated.

For an overview, Fig. 6 shows a map with all discussed major wildfire events. The Canadian fires in 2017 and the Australian fires in 2019/2020 were accompanied by pyroCb convection. Siberian fire smoke reached the stratosphere via the self-lofting process. The Kuwaiti fires in 1991 are shown for comparison as the smoke from burning oil fields has a much higher BC fraction (about 20%) than wildfire smoke (about 2.5%). The predominant burning material consists of fir, aspen, and cedar trees in the case of Canadian forest fires, and spruce, pine, and larch trees in the case of Siberian fires. In Australia, however, the oil containing eucalyptus trees might lead to more BC containing absorptive smoke aerosol compared to the Canadian and Siberian smoke layers.

Table 2 summarizes the key differences between pyroCb-related and self-lofting-related fire events. Besides the large difference in the tropospheric residence time before reaching the tropopause region (1 h versus 3-7 days), plume-like structures with an initially high AOT may prevail in the case of pyroCb lofting whereas a more homogeneous and diffuse smoke layering should be the rule for slowly ascending smoke fields. The particle linear depolarization ratio is typically around 20% at 532 nm for pyroCb-injected smoke plumes mainly consisting of irregularly shaped freshly emitted fire particles. In contrast, the particles in self-lofted smoke plumes have sufficient time to interact with tropospheric gases and to experience extensive aging. Chemical aging is assumed to lead to a spherical shape of smoke particles and thus low depolarization ratio of clearly below 5%. More details can be found in Ansmann et al. (2021b, a) and Ohneiser et al. (2021, 2022).

3.1 Impact of smoke layer AOT and layer height on heating and lofting rates

The AOT widely determines how much shortwave radiation can be absorbed and how strong an aerosol layer can heat up. In Fig. 7, a 2 km thick smoke layer is simulated. This smoke layer was parameterized in the way described in Fig. 3b, however, now for a 2 km instead of a 4 km thick layer. In the simulation, the center height of the smoke layer was stepwise increased by 1 km between 1 and 28 km height, i.e., calculations were performed for layers from 0-2 km to 27-29 km height. The layer boundaries indicate the height where the extinction coefficient starts to increase with height (layer bottom) and does not decrease with height anymore (layer top). As in Fig. 3b the AOT was scaled as indicated in the legend. Four different AOTs are assumed. In this way the difference between heating and lofting conditions in the troposphere and stratosphere become visible. As can be seen, the heating rate in Fig. 7a increases exponentially with height and approximately linearly with AOT. Every 5 km the heating rate is doubled for the same AOT. Less dense air can be heated up much more efficiently. A 2 km thick aerosol layer with an AOT of 1.5 at 1 km height is heated with $3.5\,\mathrm{K\,day^{-1}}$ while the same layer at 25 km height would heat up as much as $100\,\mathrm{K\,day^{-1}}$.

The heating rate in Fig. 7a is transferred into a lofting rate in Fig. 7b by using the gradient of the potential temperature in Fig. 5 (using the Punta Arenas January 2020 data). Generally, the lofting rate increases with increasing height in the troposphere and in the stratosphere. However, there is a pronounced lofting inhibition (minimum) at the tropopause around 12 km height. The strong increase of the gradient of the potential temperature inhibits the lofting efficiency by more than a factor of two at the tropopause compared to 8 km height. Within the stratosphere lofting rates increase again. For an aerosol optical thickness of 1.5 the lofting rate would reach $3\,\mathrm{km\,day^{-1}}$ at around 25 km height.

3.2 Impact of smoke absorption characteristics on smoke lofting

220 Figure 8 focuses on the difference in the smoke absorption characteristics. The three different black carbon parametrizations discussed in Sect. 2.4 and shown in Fig. 4 are considered. The simulations were performed with Gaussian-shaped 2-km thick profiles (vertical profile shape as in Fig. 3b, but for a 2-km deep layer) in 1 km steps up to 20 km height. Figure 8a generally shows an exponential increase of the heating rate with height. Differences in the heating rates by using the three different parameterizations become visible in the stratosphere.

225   Regarding the lofting rates, Redfern et al. (2021) showed that lofting also depends on the relative humidity as well as wind speed and wind shear. The atmospheric profiles of potential temperature gradient and the relative humidity at Punta Arenas measured on the 26 Jan 2020 are shown in Fig. 8b. The gradient of the potential temperature is around 5 K in the troposphere and around 20 K in the stratosphere up to 20 km height. In between, there is a strong change of the temperature gradient at the tropopause. The relative humidity shows an almost saturated moist layer at 1-4 km height, a dry layer between 5 and 7 km, and

230 a slightly increased relative humidity of 25% between 7 and 9 km. In the stratosphere 0-10% relative humidity was found for that day.

   The resulting lofting rates in Fig. 8c show an increase of $0.5\,\mathrm{km\,d^{-1}}$ at 1 km height to $\approx 2\,\mathrm{km\,d^{-1}}$ below the tropopause for all three BC parametrizations. At the tropopause lofting rates decrease to less than $1\,\mathrm{km\,d^{-1}}$ due to the strong increase of the potential temperature gradient. Again, higher up in the stratosphere lofting rates increase to $2\,\mathrm{km\,d^{-1}}$. Comparing the three

235 different parametrizations in Fig. 8d yields differences in the lofting rates of less than $0.3\,\mathrm{km\,d^{-1}}$. Relative uncertainties in the lofting rate simulations are smaller than 20%.

   The differences between 'BC3-BC2' as well as 'BC3-BC1' shows the obvious impact of the relatve humidity on the lofting rates. The impact is weak in the case of 'BC2-BC1'. The local maxima in the relative humidity at 2.5 km and 8 km height coincide with the local maxima in the differences of the parametrizations. This behavior reflects differences in the water

240 up take efficiency (of the smoke particles) in the different parameterizations. Different hygroscopic properties lead to slight changes in the chemical composition of the coating of the smoke particles and thus of the light-absorption properties. Smoke particles with a liquid coating may focus solar radiation to the core of the particle and increase the absorption coefficient by up to a factor of 2 (Liu and Mishchenko, 2018) which would increase the heating rate and hence lofting rate of the smoke layers. Parametrization 'BC2' is systematically slighly increased compared to 'BC1' between 0.1 and $0.2\,\mathrm{km\,d^{-1}}$ with increasing

245 humidity, potentially linked to different absorption characteristics. Nevertheless, all the differences are within a small range and it is reasonable to use BC parametrization number 1 (Hess et al., 1998).

3.3 Impact of low level clouds on smoke lofting

An additional parameter that influences the lofting rate of an aerosol layer is the fraction of clouds that are located below an aerosol layer. Solar radiation is efficiently reflected by clouds. Therefore, large fractions of the radiation are passing twice

250 through the aerosol layer and increase the heating rate significantly. Typical albedo values of the Earth's surface are around 0.3 whereas low level clouds can have an albedo of up to more than 0.9.

Figure 9 provides insight into the impact of low level clouds on the lofting of lofted layers. A smoke layer, initially centered at 4 km height after injection, is simulated. Gaussian-shaped profiles (in terms of light extinction profile) were simulated (with 2 km or 4 km thickness) and scaled to an AOT of 2. Again, the daily average heating rates (considering the Sun position every three hours from 0 UTC to 21 UTC) were used to calculate the heating rates and lofting rates. The radiation that passes through an aerosol layer during an overcast cloud situation was set to 1.7 times the initial radiation for the overcast 'c' scenario. The black and red curves represent the overcast situation and show a much larger lofting rate compared to the respective orange curve (orange curve vs red curve) that represents clear sky conditions. In an overcast situation, it takes 202 hours (8.5 days) for an aerosol layer with an AOT of constantly 2 and a layer thickness of 4 km to ascend from 4 km height to 16 km whereas it would take 344 hours (14.5 days) in a clear sky situation. Thus, a cloud layer below an absorbing aerosol layer increases the lofting rate by around 70%.

Analogously, also the layer thickness influences the lofting rate. The 4 km thick aerosol layer (red curve) shows a much lower lofting rate compared to the case with a 2 km layer geometrical thickness (black curve) and same AOT (and thus a factor of 2 higher particle extinction coefficients). During an overcast situation a 2 km thick layer would ascend from 4 to 16 km within 107 hours while a 4 km thick layer would need 202 hours.

3.4 Impact of height-dependent heating and lofting on ascending layer structures

It was shown that smoke layers have a significant lofting potential in the troposphere and the stratosphere. In the troposphere, the heating rates are comparably low but also the potential temperature gradient is low. In the stratosphere, the heating rates are much larger for the same aerosol optical thickness, however, the limiting factor, the potential temperature gradient, is also strongly enhanced. All layers have in common that they encounter meteorological stresses like wind shear and turbulence that may destroy coherent structures of an aerosol layer and the ability of a layer to efficiently ascend. Also radiative effects cause an additional stress on the aerosol layer structures.

Figure 10a shows a rectangular-shaped smoke particle extinction profile in the troposphere between 4-6 km with an average extinction coefficient of $1.2 \, \mathrm{Mm}^{-1}$. In Fig. 10f, a stratospheric smoke profile between 24-26 km with an average extinction coefficient of $0.4 \, \mathrm{Mm}^{-1}$ is simulated. The respective profiles of the heating rate in Fig. 10b and g show differential heating of the aerosol layer. The layer top is much more heated than the layer bottom. The tropospheric heating rates show values around $6 \, \mathrm{K \, day}^{-1}$ at the layer bottom and $9 \, \mathrm{K \, day}^{-1}$ at the layer top, whereas the stratospheric heating rates are $45 \, \mathrm{K \, day}^{-1}$ at layer base and $70 \, \mathrm{K \, day}^{-1}$ at layer top. In relative numbers, the heating of the layer top of the 2 km thick layer is 50% higher than heating of the layer base. However, lofting strongly depends on the potential temperature gradient as well. In the troposphere (Fig. 10c), the potential temperature gradient slightly decreased from $4.2 \, \mathrm{K \, km}^{-1}$ at 4 km height to $3.4 \, \mathrm{K \, km}^{-1}$ at 6 km height. In the stratosphere (Fig. 10h), the potential temperature gradient strongly increased from $27 \, \mathrm{K \, km}^{-1}$ at 24 km height to $31 \, \mathrm{K \, km}^{-1}$ at 26 km height. These different meteorological conditions result in differerent shapes of the lofting rate profiles in the troposphere and the stratosphere. In the troposphere (Fig. 10d), the lofting rate is almost twice as large at the layer top compared to the one at layer base, whereas in the stratosphere (Fig. 10i) the lofting rate is quite constant throughout the aerosol layer. This means that the layer top is lofted more efficiently compared to the layer base in both cases. However, this

effect is much more pronounced in the troposphere. The resulting new aerosol extinction profiles in Fig. 10e for the troposphere and in Fig. 10j for the stratosphere show the structure of the aerosol layer after one day of ascent. The tropospheric aerosol layer is now found between 4.9 km-7.8 km height. The layer depth increased by 50%. As a consequcne, the layer mean particle extinction coefficient is reduced by 30%. In contrast, the boundaries of the stratospheric layer are found between 25.2 km and

290   27.4 km. The layer thickness is only increased by 10% and the layer mean extinction coefficient decreased by only 10%.

The simulations illustrate why stratospheric layers are able to show coherent structures over long time periods compared to smoke structures in the troposphere. Tropospheric smoke layers are stretched more in vertical direction so that additional wind shear and turbulence can easily destroy coherent structures in the less stratified troposphere. Furthermore, the related stronger decrease of the layer mean extinction coefficient (of tropospheric layers) lead to smaller heating rates at the next time step and

295   therefore smaller lofting rates on the next day. All these reasons and influences must be kept in consideration when comparing CALIOP observations of tropospheric and stratospheric ascending smoke layers (and structures) with respective simulations. Self-lofting processes of smoke in the troposphere on a day by day basis is hardly observable as we will further discuss in Sect. 4.

3.5   Impact of a steadily decreasing smoke layer AOT on the ascent behavior

300   Figure 11 shows the temporal evolution of the layer center of a 2.5 km thick aerosol layer (with Gaussian-shaped aerosol profile) in dependence on the AOT. The initial layer center was at 3 km height (at day 0). The profiles were scaled to an AOT of 1, 2, and 3, as shown in the legend, analogously as compared to Fig. 3b. Three different BC fractions are considered. Again, daily-average heating rates are used and respective daily-average lofting rates are calculated. In reality, the smoke layers diverge with time so that the AOT decreases. In the scenarios in Fig. 11, the AOT decreases by 15% from day to day. On each next

305   day, the new smoke layer centre in terms of extinction is calculated from the layer center height of the last day plus the 24 h mean lofting rate. The layer thickness is always 2.5 km and the AOT is 15% less compared to the day before. All curves in Fig. 11 indicate ascending layers that accelerate in the higher troposphere although AOT is decreasing by 15% per day. At the tropopause all aerosol layers ascend slowly. The higher the BC fraction, the higher is the finally reached altitude. After 14 days of lofting, a smoke layer with a 2.5% BC content would typically be found only 1 km below the height of an aerosol layer with

310   a 3.5% BC content. A higher BC fraction is directly related to a larger ascent rate, however, there are too many free parameters that influence the ascent rate which makes it hard to determine the BC fraction from model simulations when comparing to an observed lofting rate.

We added a simulation of an ascending aerosol layer with a rather high BC fraction of 15%. In 1991, extreme oil field fires in Kuwait released large amounts of black aerosol. This aerosol absorbed 75 to 80% of solar radiation (Johnson et al., 1991;

315   Hobbs and Radke, 1992; Parungo et al., 1992). The Kuwait fire aerosols consisted of 15-20% soot, 30% organics, 8% sulfate, 30% salt, and mineral dust (Rudich et al., 2003). As can be seen, this aerosol layer with 15% BC content ascends fast. Even in the case of a low AOT of around 1 this layer would reach the stratosphere easily. The wildfire smoke AOT typically needs to be larger than 2 in cases with 2%-3.5% BC fraction to reach the tropopause level. If the AOT is even around 3 such an aerosol layer with 15% BC fraction would immediately be lofted up to 20 km height.

320   Our simulations show that it is in principle possible to loft an aerosol layer to the tropopause in the absence of any pyroCb convection. As the lofting process is quite efficient in the upper troposphere, even in the case of moderate pyroCb development with cloud tops reaching 8-10 km height only, smoke layers can easily be lofted higher up into the stratosphere.

In addition to optically thick smoke layers that ascend from the troposphere to the stratosphere, Figure 11 provides an estimate regarding the minimum AOT that is required to further loft the aerosol plume (and thus to dominate over downward
325   motion by sedimentation). The red lines represent a smoke layer in the stratosphere at 13 km height (day 0) with an initial AOT of 1, 0.5, and 0.1 at 532 nm. Every day, the AOT reduces by 15%. As can be seen, for an AOT of 1 the smoke layer ascends about 3.2 km in two weeks. For an AOT of 0.5 the ascent is reduced to 1.7 km within two weeks. For an initial AOT of 0.1 the height gain is about 600 m within 14 days or 43 m per day. Further simulations with an AOT of 0.05 and 0.01 yield ascent rates of 30 m and 15 m per day. However, it must be noted that these values are representative for a 2.5 km thick smoke layer
330   at 13 km. Smoke layers with a layer thickness of 10 km or 15 km, as it was observed for the Siberian and Australian wildfire smoke would be lofted around 4 m and 3 m per day, respectively, for an AOT of 0.01. During the autumn and winter months this ascent rate is even lower. Therefore, for such a small AOT of 0.01 and lower, the sedimentation of the smoke particles in the stratosphere would dominate the self-lofting process. After the strong Pinatubo volcanic eruption in June 1991, we observed an average descent rate of the stratospheric Pinatubo layer center of about 5-6 m per day from 1992-1994 (4 km in 750 days)
335   (Ansmann et al., 1997).

3.6   Summary of simulation uncertainties

The self-lofting efficiency for given smoke layers depend on many factors. The most important parameters are summarized in Table 1. The aerosol optical thickness plays a key role in lofting aerosol layers. Usually an AOT of >0.5 in the stratosphere or >2 in the troposphere is necessary in order to significantly loft smoke plumes by a few kilometers. A doubling in AOT means
340   a doubling in heating rate and hence lofting rate (thus the impact is described as linear in Table 1). Also the layer thickness sensitively influences the lofting rate. If the same AOT is distributed over a larger vertical column, the layer mean particle extinction coefficient and the corresponding heating rate is decreased and therefore the lofting rate is decreased.

Another indirect effect (caused by vertical stretching) is the increasing impact of vertical wind shear with increasing vertical extent of the smoke plumes. Wind shear can effectively destroy the aerosol layer structures and can sigificantly reduce the
345   lifetime of the layer. The height of a smoke plume itself is relevant for the lofting rate. The higher the smoke plume center height, the higher is the heating rate. As discussed in Sect. 3 the heating rate is approximately doubled at every 5 km height step. Thus this impact is described as nonlinear in Table 1.

The lowest troposphere and the tropopause are height regions which allow only for comparably small lofting rates. Furthermore, it is important to note that the initial smoke layer height (meaning the injection height) needs to be precisely known for
350   long-lived smoke plumes. Especially in the stratosphere the underestimation/overestimation of the injection height leads to an underestimated/overestimated lofting rate which defines the new height of the next iteration step. The wrong estimation will sum up in every step. As will be shown in Sect. 4.3 for the Australian wildfire smoke an injection at 1 km higher altitude would

lead to an additional lofting of 5 km. As discussed, the lofting rate is strongly dependent on the layer height itself, so the error will not linearly sum up but exponentially to some extent.

355 The BC/OC ratio is usually around 2.5% which is the main driver for the self-lofting process. The higher the BC/OC ratio is, the larger is the lofting rate. Not only the BC/OC ratio but also the parameterized optical properties of the BC aerosol have an impact on the modeled lofting rate. The single scattering albedo as well as the asymmetry factors can vary slightly depending on the concrete case. Depending on the forest type, as well as the fire type (discussed in Ohneiser et al. (2020)) each fire aerosol event can evolve different wildfire aerosol particles in terms of absorbing characteristics of the BC particles (see Sect. 3). Slight

360 changes in SSA and g can already create 10% of uncertainty in the lofting rate calculations.

Also the atmospheric situation itself can significantly contribute to the lofting of smoke layers. Clouds above the aerosol layer will decrease the amount of radiation and hence the lofting rate of smoke particles. Smoke above a reflecting cloud layer will lead to an almost doubled lofting rate as the shortwave radiation is reflected by the clouds and enters the smoke layer twice. This process is especially important in the stratosphere.

365 Increased atmospheric relative humidity can lead to a liquid coating of the BC/OC aerosol mixtures, especially in the troposphere. This has also slight influence on the absorption of shortwave radiation, depending on the black carbon type. Smoke particles in the troposphere with a liquid coating may focus solar radiation to the core of the particle.

All these uncertainties do not cancel out each other. Uncertainties can sum up with travel time (time for lofting). The calculated layer heights can significantly deviate from observations after 10-20 days. Thus, it remains difficult to reproduce

370 observed lofting behavior (especially in the troposphere, as discussed below) and it is even more difficult to forecast the behavior of a strong, optically dense smoke plume that may have a lifetime of more than two months. Slight changes in the initial smoke plume characteristics can lead to significant differences in the heights at which a strong smoke plume can be found after a few weeks. However, the next section demonstrates that the presented ECRAD-based simulation tool is a powerful instrument to explain self-lofting as observed with the spaceborne CALIOP lidar.

375 4 Comparison of CALIOP smoke observations with ECRAD simulations

4.1 Observational data sources

To check the usefulness and applicability of the developed ECRAD-based self-lofting simulation scheme we compared smoke self-lofting events as observed with the spaceborne CALIOP lidar with respective simulation results. In Sect. 4.2 and 4.3, two cases of stratospheric smoke layers (Canadian smoke in 2017, Australian smoke in 2020) are discussed. Ascent rates of

380 tropospheric smoke layers (over Siberia in 2019 and 2021) are presented in Sect. 4.4. The general strategy was to determine (or estimate) the geometrical properties of the detected smoke layers (layer depth, center, top and base heights) as well as the AOT values, from the CALIOP observations on a daily basis. These data were then used as input in the simulations. The lofting rates as observed with CALIOP were finally compared with simulated lofting rates. As a free parameter, we adjusted the BC fraction in the simulations to optimize the match between simulated and observed ascending smoke features.

385 CALIOP quicklooks (colored height-time displays of the attenuated backscatter coefficient at 532 nm) were downloaded CALIPSO (2022) and displayed in time series over days to weeks (see for example Fig. 12). Layer bottom and top heights were determined by visual inspection of the backscatter features. With the layer base and top height information, the height of the layer center is obtained. Furthermore, AOT was estimated from the total (Rayleigh plus particle) attenuated backscatter profiles. A small stratospheric Rayleigh AOT contribution of the order of 0.005 at 532 nm was ignored. The AOT is calculated

390 from the layer mean attenuated backscatter coefficient multiplied by a typical smoke lidar ratio of 65 sr, 85 sr, and 91 sr for the Canadian, Siberian, and Australian wildfire smoke (Baars et al., 2019; Ohneiser et al., 2021, 2022), respectively, and finally multiplied by the layer geometrical depth. This AOT value may underestimate the true AOT by 50% when using attenuated backscatter information instead of the true particle backscatter coefficient profile and by ignoring multiple scattering effects in the retrieval. Therefore, we considered also AOT values multiplied by a factor of 1.5 as input in subsequent simulations.

395 For stratospheric smoke layers this procedure is straight forward. In the troposphere, however, the less coherent aerosol layer structures are often hard to identify on a daily basis (see discussion in Sect. 4.4). Therefore, the layer center of detected smoke structures was set to the height where the signal maximum was found. The vertical extent of the smoke layer was then roughly estimated again by visual inspection of the backscatter color plots. The AOT information was then estimated in the same way as described above for the stratospheric layers.

400 In addition, MODIS (Moderate Resolution Imaging Spectroradiometer) data (MODIS, 2022) were used in the case of Australian smoke scenarios as independent approach to obtain smoke AOT information. MODIS AOT values are more reliable but contain information about the entire vertical column including contributions of aerosol particles in the lower troposphere of the order of 0.02-0.06 over the southern Pacific and Southern Ocean.

4.2 Ascending Canadian wildfire smoke in the stratosphere

405 Khaykin et al. (2018), Baars et al. (2019), Torres et al. (2020), and Lestrelin et al. (2021) discussed cases with ascending stratospheric Canadian wildfire smoke detected in the summer of 2017. Figure 12a-g shows CALIOP measurements of an ascending Canadian smoke plume between 14 August 2017 and 4 September 2017. Within 21 days the smoke layer ascended by self-lofting processes by 6 km. In the beginning, the smoke plume height increased from around 12 km on 14 August 2017 to around 16 km on 19 August 2017. The lofting rate was thus almost 1 km per day. The particle attenuated backscatter coefficients

410 in the layer slowly decreased with time from values $>5\,\mathrm{Mm}^{-1}\,\mathrm{sr}^{-1}$ to values around $1\,\mathrm{Mm}^{-1}\,\mathrm{sr}^{-1}$. With decreasing backscatter (and light-absorption) the height gain decreased as well. Within the following 16 days the height of the smoke plume increased from 16 km on 18 August 2017 to 19 km on 4 September 2017.

In Fig. 13a and b, the layer thickness and AOT estimated from the CALIOP observations are shown. In addition, the parameterization of the geometrical and optical properties as used as input in the ECRAD simulations are presented. As mentioned,

415 the stratospheric AOT obtained from the CALIOP observations may not reflect the truth. Therefore, we used two AOT parameterizations. The simulation results regarding self-lofting are shown in Fig. 13c together with the smoke lofting behavior as observed with CALIOP. A BC fraction of 2.5% was assumed in the simulations. The match with the observations is obtained

for the 1.5 AOT values. Obviously the ECRAD simulation tool allows us to realistically describe heating rates and self-lofting processes.

4.3 Ascending Australian wildfire smoke in the stratosphere

Ohneiser et al. (2020, 2022), Kablick et al. (2020), Khaykin et al. (2020), and Allen et al. (2020) studied the ascent behavior of the Australian smoke layer in 2020. Here, we deepen this discussion. In Fig. 16a-j, CALIOP observations of Australian fire smoke are shown. From 31 December 2019 to 5 January 2020, extremely intense fires over large areas in southeastern Australia in combination with the evolution of more than 40 individual pyrocumulonimbus storms (Peterson et al., 2021; Ohneiser et al., 2022) caused the injection of record-breaking amounts of fire smoke into the UTLS region. Extended smoke fields were detected at 14 km height on 31 December 2019 (Fig. 13h). During the first 12 days after injection, the smoke layer ascended and reached the 20 km level on 11 January 2020. Similarly to the Canadian stratospheric fire smoke, the aerosol backscatter decreased from values $>5\,\mathrm{Mm^{-1}\,sr^{-1}}$ in the beginning of January to values $<0.5\,\mathrm{Mm^{-1}\,sr^{-1}}$ mid of February. In contrast to the Canadian fire smoke plume, the Australian smoke plume remained compact and as a consequence, ascended more efficiently over weeks. During the following 30 days the smoke layer reached almost the 30 km height level.

More details of the ascending Australian smoke layers are given in Fig. 15. The figure is in full agreement with the results shown by Kablick et al. (2020) and Khaykin et al. (2020). However, we went through all CALIOP observations again and independently obtained a detailed lofting data set that can be used in our simulations and comparisons with the CALIOP observations. The temporal evolution and corresponding geolocation and height information of the two most pronounced Australian fire smoke plume events are shown in Fig. 15a and b. The smoke plumes (injected from 31 December to 5 January) split up into two parts between 3 and 6 January 2020. One part of the plume shown in Fig. 15a took a route from Australia to the southernmost tip of South America. During the travel, the smoke field continuously ascended (Fig. 15c). When the smoke plume was close to South America, the 26-28 km height zone was reached in which the wind velocity was very low. The smoke plume remained close to the southernmost tip of South America for around one week. By further lofting, the aerosol field entered the easterly wind regime and started to move towards the west, passed New Zealand and the region south of Australia during the following weeks, and reached heights of >30 km (Fig. 15c) near South Africa.

The second part of the initial smoke field in Fig. 15b took a southern route over Antarctica. As can be seen in Fig. 15c, also this layer gained height continuously, almost as fast as the other part of the plume. In mid February 2020, the second part of the plume was detected south of South America at around 26 km height and then started to cross the southern Atlantic towards Africa.

During the travel, the layer thickness increased and AOT decreased. The smoke layer thickness of the first part of the smoke layer (Fig. 15a) retrieved from the CALIOP observations is shown in Fig. 16a. Initially, the smoke layer thickness was around 3-5 km and increased to 6-8 km after a month. The AOT in Fig. 16b is calculated by using CALIOP and MODIS data. The CALIOP AOT data were taken from Kablick et al. (2020). The parameterization is mostly based on the AOT maxima because we assume that the highest AOTs may best represent the optically dense center region of the smoke field. We used MODIS observations as an independent approach to obtain an AOT time series (for 550 nm wavelength) along the smoke travel pathway.

We did not subtract a minor AOT contribution of 0.03-0.05 for tropospheric aerosols. As can be seen in Fig. 16b the MODIS-derived AOTs are around 3 times as high as the CALIOP AOT values. Both AOT parameterizations shown in Fig. 16b as solid lines were then used in the model calculations presented in Fig. 16c.

455   The comparisons in Fig. 16c reveal that the smoke lofting as observed with CALIOP (dashed black line) cannot be reproduced by means of the CALIOP AOT time series (blue line) in combination with a BC fraction of 2.5%. All the other simulations were based on the MODIS AOT parameterization. With the MODIS AOT data a good match with the CALIOP observations is obtained for a BC fraction of 2.5%, however, not for 1.5% and 3.5% BC fractions. The self-lofting is underestimated by around 3 km after 2 months when assuming an 1.5% BC fraction. For 3.5% BC fraction the self-lofting is
460   overestimated by around 5 km after 2 months. The scenario with 2.5% BC fraction fits very well to the observations at all times. This finding is in agreement with studies of Yu et al. (2019, 2021) and Torres et al. (2020) who also concluded that the BC fraction must be around 2.5% to explain the observed smoke lofting of stratospheric wildfire smoke layers.

Especially the decreasing lofting rate is well-captured by the simulations and the final height at 30 km after 2 months is in full agreement with the observations. This shows that our ECRAD-based simulation scheme can reproduce the observed lofting
465   rates of the smoke plumes. However, there are a lot of parameters to be set that can sensitively influence the simulations. For example, the grey curve (BC25_hypo) shows the same simulation as the well-fitting scenario with the MODIS AOT parametrization and 2.5% BC fraction. The only difference is that the injection height was moved upward from 14 to 15 km height. This hypothetical calculation shows once more how sensitive the self-lofting effect is to slight changes of any parameter. The final height after 2 months is around 6 km higher if the initial injection height is 1 km higher and all other settings remain
470   unchanged. This large sensitivity of the injection height was also shown in Heinold et al. (2021).

As was discussed in Sect. 3.1 and presented in Fig. 7, for a given AOT the self-lofting rate increases with height within the stratosphere. Especially for long-lived smoke plumes, all these influences of given uncertainties in the simulation input parameters may sum up to several-kilometer height differences. In fire events, similar to the Australian smoke events with smoke, however, with injection heights 1-2 km higher up, a slightly increased AOT, and a 0.5% higher BC fraction, the smoke
475   could potentially reach heights that are more than 10 km higher than observed with CALIOP in January and February 2020 over the Southern Ocean.

4.4 Self-lofting of tropospheric wildfire smoke layers over Siberia in 2019 and 2021

The study of tropospheric smoke lofting is difficult. The reasons were discussed in Sect. 3.4. Coherent structures can immediately get lost due the impact of wind shear, local turbulence, and height-dependent heating (Fig. 10). Here, we discuss two
480   cases of self-lofting of tropospheric smoke layers observed over central and eastern Siberia in 2019 and 2021. Figure 17 shows the respective CALIOP observations. Almost coherent smoke plume structures could be observed from 12 August to 15 August 2019 (Fig. 17a-d). The smoke at different heights was transported in the same air column. The trajectories analysis in Fig. 18a indicated similar wind speed and directions at different heights in the middle troposphere. The smoke slowly ascended from around 3-4 km height to 5-6 km height. The backward trajectories (not shown) indicate no direct link of the air mass at 5-6 km
485   height with lower heights (and thus a direct fire smoke uptake from the sources). Thus, lofting effects obviously caused the

pollution in the middle troposphere. The observation were taken over the East Siberian Sea north of Siberia (78°N, 160°E). The black dots indicate the position of the smoke layer center each 24 h as observed with CALIOP and shown in Fig. 17, the numbers indicate the height of the layer centre.

In 2021, complex smoke structures were observed. We used the CALIOP observations from 4 August to 10 August 2021 to link similar smoke features (Fig. 17e-j). The corresponding forward trajectories in Fig. 18b show that the air masses at different heights again belong to the same tropospheric vertical air column so that smoke structures at different heights were probably connected via self-lofting. The backward trajetories at 7 and 9 km height (not shown) did not indicate direct smoke uptake over fire areas in Siberia. The backward trajectories arriving at 7 and 9 km were all at heights above 7 km during the last 10 days. Initial smoke plumes were at around 3 km height on 4 August 2021. The same structures were found everyday in the following days in the same area, being located at 6-7 km on 6 August 2021 and at 9-10 km on 10 August 2021. Fractions of this smoke plume must have reached the tropopause and later on the lowest stratosphere. These observations were used for the model simulations summarized in Fig. 19.

Figures 19a and b show the layer thickness and the AOT, respectively, estimated from the CALIOP observations in Fig. 17. Both smoke events (2019, 2021) are shown in the same figure. The layer thickness was usually between 2-4 km in both cases. The AOT in Fig. 19b shows initial values of 0.5 to 0.8 in 2019 that decreased to around 0.2 after 6 days. In 2021, initial AOT values were between 0.6 and 1 and decreased to around 0.2 after a week. Again, in both cases it is supposed that the AOT was underestimated and therefore the AOT was also multiplied by 1.5 in the model simulations in Fig. 19c.

In 2019, the model results in Fig. 19c agree well with CALIOP observations. The model simulation with 2.5% BC fraction yield slightly lower smoke center heights as observed with CALIOP. The simulation with 3.5% fits better to the observations. In 2021, the model simulations underestimate the observed self-lofting. However, the general lofting behavior (5 km ascent in 6 days) as observed could well be simulated. Again, the simulations with a 3.5% BC fraction as input parameter fits better to the observations.

The model simulations in the troposphere show higher uncertainties than the stratospheric simulations. As explained, because of the potentially complex meteorological conditions including not well known details of the temperature profiles and gradients above the fire areas it is almost impossible to accurately simulate tropospheric self-lofting processes. However, for the first time, such an attempt was undertaken here and reasonable agreement of simulations with observations was obtained. We can conclude that even tropospheric smoke can ascend significantly from lower tropospheric injection heights up to the tropopause level within a few days and even enter the lower stratosphere as demonstrated in Ohneiser et al. (2021).

5 Summary and outlook

We presented the ECRAD-based simulation scheme that allows us to estimate the self-lofting rate of smoke layers caused by heating due to absorption of solar radiation by smoke particles leading to the subsequent ascent of the layer in the troposphere and stratosphere. We discussed the influence of uncertainties in the required input parameters such as AOT, layer thickness and height, absorption properties of smoke particles, and of atmospheric parameters (cloudiness, relative humidity, potential

temperature gradient) on the self-lofting results. Uncertainties in the simulated heating and lofting rates of 30% and 50% can
520 easily be caused by not well known and considered input datameters.

The main findings of this study were that:

- smoke layers can reach the tropopause via the self-lofting effect within 3-7 days in the absence of pyroCB convection if the
AOT is larger than approximately 2 for a longer time period.

- once in the stratosphere, self-lofting dominates over sedimenation as long as the AOT is > 0.01 at 532 nm.

525 - the large number of open parameters generates large uncertainty / sensitivity to the modeled lofting rates.

In several case studies with Canadian and Australian smoke in the stratosphere and Siberian smoke in the troposphere,
good agreement between the ECRAD-based simulations of smoke lofting and the smoke ascent behavior observed with the
spaceborne lidar CALIOP was obtained and indicates the applicability of the model to realistically simulate smoke ascent rates
530 over weeks to months.

An open issue is the proper consideration of smoke optical properties in the simulations. More laboratory efforts and air-
borne in situ observations of aged smoke are required to improve our knowledge about relationships between the chemical
composition (including a better understanding regarding internal vs external mixing) and microphyscial properties (size distri-
bution, shape features), as well as light-scattering and absorption properties of aged smoke particles after long-range transport
535 over weeks to months.

6 Data availability

CALIPSO observations were downloaded from the CALIPSO data base (CALIPSO, 2022). Polly lidar observations (level 0
data, measured signals) are in the PollyNet database (Polly, 2022). The radiosonde data are available at Uni-Wyoming (2022).
CAMS data are available on the Copernicus website CAMS (2022). MODIS data are available at the NASA data base MODIS
540 (2022). Forward trajectory analysis has been performed by air mass transport computation with the NOAA (National Oceanic
and Atmospheric Administration) HYSPLIT (HYbrid Single-Particle Lagrangian Integrated Trajectory) model (HYSPLIT,
2022).

7 Author contributions

The paper was written and designed by KO and AA. The model simulations and data analysis were performed by KO, AA,
545 JW, and GW, supported by HD and AC (MODIS data analysis). All co-authors contributed to the discussion of the results.

8 Competing interests

The authors declare that they have no conflict of interest.

9 Financial support

The authors acknowledge support through the European Research Infrastructure for the observation of Aerosol, Clouds and
550   Trace Gases ACTRIS under grant agreement no. 654109 and 739530 from the European Union's Horizon 2020 research and
innovation programme. The field observations at Punta Arenas were partly funded by the German Science Foundation (DFG)
project PICNICC with project number 408008112. This research has been supported by the U.S. National Science Foundation
(grant no. AGS-1446286) and the U.S. Department of Energy, Office of Science (BER), Atmospheric System Research (grant
no. DE-SC0021034). The Polarstern Polly data was produced as part of the international Multidisciplinary drifting Observatory
555   for the Study of the Arctic Climate (MOSAiC) with the tag MOSAiC20192020 and Project ID AWI_PS122_00.

Acknowledgements.   We are greatful to the entire research team (University Magellan, Leipzig University, TROPOS) to make the three-year
DACAOPO-PESO campaign to a big success. We are grateful to the CALIPSO team for their well-organized easy-to-use internet platforms.

References

Allen, D. R., Fromm, M. D., III, G. P. K., and Nedoluha, G. E.: Smoke with Induced Rotation and Lofting (SWIRL) in the Stratosphere,
560   Journal of the Atmospheric Sciences, 77, 4297 – 4316, https://doi.org/10.1175/JAS-D-20-0131.1, 2020.

Ansmann, A., Mattis, I., Wandinger, U., Wagner, F., Reichardt, J., and Deshler, T.: Evolution of the Pinatubo aerosol: Raman lidar observa-
    tions of particle optical depth, effective radius, mass, and surface area over Central Europe at 53.4°N, Journal of the Atmospheric Sciences,
    54, 2630 – 2641, https://doi.org/10.1175/1520-0469(1997)054<2630:EOTPAR>2.0.CO;2, 1997.

Ansmann, A., Ohneiser, K., Chudnovsky, A., Baars, H., and Engelmann, R.: CALIPSO Aerosol-Typing Scheme Misclassi-
565   fied Stratospheric Fire Smoke: Case Study From the 2019 Siberian Wildfire Season, Frontiers in Environmental Science, 9,
    https://doi.org/10.3389/fenvs.2021.769852, 2021a.

Ansmann, A., Ohneiser, K., Mamouri, R.-E., Knopf, D. A., Veselovskii, I., Baars, H., Engelmann, R., Foth, A., Jimenez, C., Seifert, P., and
    Barja, B.: Tropospheric and stratospheric wildfire smoke profiling with lidar: mass, surface area, CCN, and INP retrieval, Atmospheric
    Chemistry and Physics, 21, https://doi.org/10.5194/acp-21-9779-2021, 2021b.

570 Ansmann, A., Ohneiser, K., Chudnovsky, A., Knopf, D. A., Eloranta, E. E., Villanueva, D., Seifert, P., Radenz, M., Barja, B., Zamorano,
    F., Jimenez, C., Engelmann, R., Baars, H., Griesche, H., Hofer, J., Althausen, D., and Wandinger, U.: Ozone depletion in the Arctic and
    Antarctic stratosphere induced by wildfire smoke, Atmospheric Chemistry and Physics Discussions, 22, https://doi.org/10.5194/acp-2022-
    247, 2022.

Baars, H., Ansmann, A., Ohneiser, K., Haarig, M., Engelmann, R., Althausen, D., Hanssen, I., Gausa, M., Pietruczuk, A., Szkop, A., Stach-
575   lewska, I. S., Wang, D., Reichardt, J., Skupin, A., Mattis, I., Trickl, T., Vogelmann, H., Navas-Guzmán, F., Haefele, A., Acheson, K., Ruth,
    A. A., Tatarov, B., Müller, D., Hu, Q., Podvin, T., Goloub, P., Veselovskii, I., Pietras, C., Haeffelin, M., Fréville, P., Sicard, M., Comerón,
    A., Fernández García, A. J., Molero Menéndez, F., Córdoba-Jabonero, C., Guerrero-Rascado, J. L., Alados-Arboledas, L., Bortoli, D.,
    Costa, M. J., Dionisi, D., Liberti, G. L., Wang, X., Sannino, A., Papagiannopoulos, N., Boselli, A., Mona, L., D'Amico, G., Romano,
    S., Perrone, M. R., Belegante, L., Nicolae, D., Grigorov, I., Gialitaki, A., Amiridis, V., Soupiona, O., Papayannis, A., Mamouri, R.-E.,
580   Nisantzi, A., Heese, B., Hofer, J., Schechner, Y. Y., Wandinger, U., and Pappalardo, G.: The unprecedented 2017–2018 stratospheric
    smoke event: decay phase and aerosol properties observed with the EARLINET, Atmospheric Chemistry and Physics, 19, 15 183–15 198,
    https://doi.org/10.5194/acp-19-15183-2019, 2019.

Barlakas, V., Deneke, H., and Macke, A.: The sub-adiabatic model as a concept for evaluating the representation and radiative effects of
    low-level clouds in a high-resolution atmospheric model, Atmospheric Chemistry and Physics, 20, 303–322, https://doi.org/10.5194/acp-
585   20-303-2020, 2020.

Barrientos-Velasco, C., Deneke, H., Hünerbein, A., Griesche, H. J., Seifert, P., and Macke, A.: Radiative closure and cloud effects on the
    radiation budget based on satellite and ship-borne observations during the Arctic summer research cruise PS106, Atmospheric Chemistry
    and Physics Discussions, 2022, 1–71, https://doi.org/10.5194/acp-2021-1004, 2022.

Boers, R., de Laat, A. T., Stein Zweers, D. C., and Dirksen, R. J.: Lifting potential of solar-heated aerosol layers, Geophysical Research
590   Letters, 37, https://doi.org/https://doi.org/10.1029/2010GL045171, 2010.

Bond, T. and Bergstrom, R. W.: Light Absorption by Carbonaceous Particles: An Investigative Review, Aerosol Science and Technology, 40,
    27–67, https://doi.org/10.1080/02786820500421521, 2006.

Bond, T. C., Doherty, S. J., Fahey, D. W., Forster, P. M., Berntsen, T., DeAngelo, B. J., Flanner, M. G., Ghan, S., Kärcher, B., Koch, D.,
    Kinne, S., Kondo, Y., Quinn, P. K., Sarofim, M. C., Schultz, M. G., Schulz, M., Venkataraman, C., Zhang, H., Zhang, S., Bellouin, N.,

595   Guttikunda, S. K., Hopke, P. K., Jacobson, M. Z., Kaiser, J. W., Klimont, Z., Lohmann, U., Schwarz, J. P., Shindell, D., Storelvmo, T.,
        Warren, S. G., and Zender, C. S.: Bounding the role of black carbon in the climate system: A scientific assessment, Journal of Geophysical
        Research: Atmospheres, 118, 5380–5552, https://doi.org/https://doi.org/10.1002/jgrd.50171, 2013.

CALIPSO(2022): CALIPSO data, available at: https://www-calipso.larc.nasa.gov/tools/data_avail/, last access: 21 February, 2022.

CAMS(2022): CAMS data, available at: https://ads.atmosphere.copernicus.eu/about-cams, last access: 21 February, 2022.

600   Chudnovsky, A. and Kostinski, A.: Secular changes in atmospheric turbidity over Iraq and a possible link to military activity, Remote Sensing,
        12, 1526, https://doi.org/10.3390/rs12091526, 2020.

Daerden, F., Whiteway, J. A., Neary, L., Komguem, L., Lemmon, M. T., Heavens, N. G., Cantor, B. A., Hébrard, E., and Smith,
        M. D.: A solar escalator on Mars: Self-lifting of dust layers by radiative heating, Geophysical Research Letters, 42, 7319–7326,
        https://doi.org/https://doi.org/10.1002/2015GL064892, 2015.

605   Dahlkötter, F., Gysel, M., Sauer, D., Minikin, A., Baumann, R., Seifert, P., Ansmann, A., Fromm, M., Voigt, C., and Weinzierl, B.: The
        Pagami Creek smoke plume after long-range transport to the upper troposphere over Europe - aerosol properties and black carbon mixing
        state, Atmospheric Chemistry and Physics, 14, 6111–6137, https://doi.org/10.5194/acp-14-6111-2014, 2014.

Das, S., Colarco, P. R., Oman, L. D., Taha, G., and Torres, O.: The long-term transport and radiative impacts of the 2017 British Columbia py-
        rocumulonimbus smoke aerosols in the stratosphere, Atmospheric Chemistry and Physics, 21, 12 069–12 090, https://doi.org/10.5194/acp-
610   21-12069-2021, 2021.

de Laat, A. T. J., Stein Zweers, D. C., Boers, R., and Tuinder, O. N. E.: A solar escalator: Observational evidence of the self-lifting of smoke
        and aerosols by absorption of solar radiation in the February 2009 Australian Black Saturday plume, Journal of Geophysical Research:
        Atmospheres, 117, https://doi.org/https://doi.org/10.1029/2011JD017016, 2012.

ECRAD(2022): ECMWF Radiation scheme home, available at: https://confluence.ecmwf.int/display/ECRAD, last access: 21 February, 2022.

615   Engelmann, R., Ansmann, A., Ohneiser, K., Griesche, H., Radenz, M., Hofer, J., Althausen, D., Dahlke, S., Maturilli, M., Veselovskii, I.,
        Jimenez, C., Wiesen, R., Baars, H., Bühl, J., Gebauer, H., Haarig, M., Seifert, P., Wandinger, U., and Macke, A.: Wildfire smoke, Arctic
        haze, and aerosol effects on mixed-phase and cirrus clouds over the North Pole region during MOSAiC: an introduction, Atmospheric
        Chemistry and Physics, 21, https://doi.org/10.5194/acp-21-13397-2021, 2021.

Fromm, M., Lindsey, D. T., Servranckx, R., Yue, G., Trickl, T., Sica, R., Doucet, P., and Godin-Beekmann, S.: The Untold Story of Pyrocu-
620   mulonimbus, Bulletin of the American Meteorological Society, 91, 1193 – 1210, https://doi.org/10.1175/2010BAMS3004.1, 2010.

Fromm, M. D. and Servranckx, R.: Transport of forest fire smoke above the tropopause by supercell convection, Geophysical Research
        Letters, 30, https://doi.org/https://doi.org/10.1029/2002GL016820, 2003.

Gasteiger, J., Groß, S., Sauer, D., Haarig, M., Ansmann, A., and Weinzierl, B.: Particle settling and vertical mixing in the Saha-
        ran Air Layer as seen from an integrated model, lidar, and in situ perspective, Atmospheric Chemistry and Physics, 17, 297–311,
625   https://doi.org/10.5194/acp-17-297-2017, 2017.

Hanschmann, T., Deneke, H., Roebeling, R., and Macke, A.: Evaluation of the shortwave cloud radiative effect over the ocean by use of ship
        and satellite observations, Atmospheric Chemistry and Physics, 12, 12 243–12 253, https://doi.org/10.5194/acp-12-12243-2012, 2012.

Heinold, B., Baars, H., Barja, B., Christensen, M., Kubin, A., Ohneiser, K., Schepanski, K., Schutgens, N., Senf, F., Schrödner, R., Vil-
        lanueva, D., and Tegen, I.: Important role of stratospheric injection height for the distribution and radiative forcing of smoke aerosol from
630   the 2019/2020 Australian wildfires, Atmospheric Chemistry and Physics Discussions, 2021, 1–20, https://doi.org/10.5194/acp-2021-862,
        2021.

Hess, M., Koepke, P., and Schult, I.: Optical Properties of Aerosols and Clouds: The Software Package OPAC, Bulletin of the American Meteorological Society, 79, 831 – 844, https://doi.org/10.1175/1520-0477(1998)079<0831:OPOAAC>2.0.CO;2, 1998.

Hicke, J., Tuck, A., and Vömel, H.: Lower stratospheric radiative heating rates and sensitivities calculated from Antarctic balloon observations, Journal of Geophysical Research, 104, 9293–9308, 1999.

Hirsch, E. and Koren, I.: Record-breaking aerosol levels explained by smoke injection into the stratosphere, Science, 371, 1269–1274, https://doi.org/10.1126/science.abe1415, 2021.

Hobbs, P. V. and Radke, L. F.: Airborne Studies of the Smoke from the Kuwait Oil Fires, Science, 256, 987–991, https://doi.org/10.1126/science.256.5059.987, 1992.

Hogan, R. J. and Bozzo, A.: A Flexible and Efficient Radiation Scheme for the ECMWF Model, Journal of Advances in Modeling Earth Systems, 10, 1990–2008, https://doi.org/https://doi.org/10.1029/2018MS001364, 2018.

HYSPLIT(2022): Hybrid Single-Particle Lagrangian Integrated Trajectory data, available at: https://www.ready.noaa.gov/hypub-bin/trajtype.pl?runtype=archive, last access: 11 April, 2022.

Jacobson, M.: Strong radiative heating due to the mixing state of black carbon in atmospheric aerosols, Nature Communications, https://doi.org/https://doi.org/10.1038/35055518, 2001.

Johnson, D., Kilsby, C., McKenna, D., Saunders, R., Jenkins, G., Smith, F., and Foot, J.: Airborne observations of the physical and chemical characteristics of the Kuwait oil smoke plume, Nature Communications, https://doi.org/https://doi.org/10.1038/353617a0, 1991.

Jolly, W. M., Cochrane, M. A., Freeborn, P. H., Holden, Z. A., Brown, T. J., Williamson, G. J., and Bowman, D. M. J. S.: Climate-induced variations in global wildfire danger from 1979 to 2013, Nature Communications, https://doi.org/https://doi.org/10.1038/ncomms8537, 2015.

Kablick, G. P., Allen, D. R., Fromm, M. D., and Nedoluha, G. E.: Australian PyroCb Smoke Generates Synoptic-Scale Stratospheric Anticyclones, Geophysical Research Letters, 47, e2020GL088 101, https://doi.org/https://doi.org/10.1029/2020GL088101, 2020.

Kanitz, T., Ansmann, A., Seifert, P., Engelmann, R., Kalisch, J., and Althausen, D.: Radiative effect of aerosols above the northern and southern Atlantic Ocean as determined from shipborne lidar observations, Journal of Geophysical Research: Atmospheres, 118, 12,556–12,565, https://doi.org/https://doi.org/10.1002/2013JD019750, 2013.

Khaykin, S., Legras, B., Bucci, S., Sellitto, P., Isaksen, L., Tencé, L., Bekki, S., Bourassa, A., Rieger, L., Zawada, D., Jumelet, J., and Godin-Beekmann, S.: The 2019/20 Australian wildfires generated a persistent smoke-charged vortex rising up to 35 km altitude, Nature Communications Earth and Environment, https://doi.org/https://doi.org/10.1038/s43247-020-00022-5, 2020.

Khaykin, S. M., Godin-Beekmann, S., Hauchecorne, A., Pelon, J., Ravetta, F., and Keckhut, P.: Stratospheric smoke with unprecedentedly high backscatter observed by lidars above southern France, Geophysical Research Letters, 45, 1639–1646, https://doi.org/10.1002/2017GL076763, 2018.

Kloss, C., Berthet, G., Sellitto, P., Ploeger, F., Bucci, S., Khaykin, S., Jégou, F., Taha, G., Thomason, L. W., Barret, B., Le Flochmoen, E., von Hobe, M., Bossolasco, A., Bègue, N., and Legras, B.: Transport of the 2017 Canadian wildfire plume to the tropics via the Asian monsoon circulation, Atmospheric Chemistry and Physics, 19, 13 547–13 567, https://doi.org/10.5194/acp-19-13547-2019, 2019.

Lack, D. A. and Cappa, C. D.: Impact of brown and clear carbon on light absorption enhancement, single scatter albedo and absorption wavelength dependence of black carbon, Atmospheric Chemistry and Physics, 10, 4207–4220, https://doi.org/10.5194/acp-10-4207-2010, 2010.

Lesins, G., Chylek, P., and Lohmann, U.: A study of internal and external mixing scenarios and its effect on aerosol optical properties and direct radiative forcing, Journal of Geophysical Research: Atmospheres, 107, AAC 5–1–AAC 5–12, https://doi.org/https://doi.org/10.1029/2001JD000973, 2002.

Lestrelin, H., Legras, B., Podglajen, A., and Salihoglu, M.: Smoke-charged vortices in the stratosphere generated by wildfires and their behaviour in both hemispheres: comparing Australia 2020 to Canada 2017, Atmospheric Chemistry and Physics, 21, 7113–7134, https://doi.org/10.5194/acp-21-7113-2021, 2021.

Liu, L. and Mishchenko, M. I.: Scattering and radiative properties of complex soot and soot-containing aggregate particles, Journal of Quantitative Spectroscopy and Radiative Transfer, 106, 262–273, https://doi.org/https://doi.org/10.1016/j.jqsrt.2007.01.020, 2007.

Liu, L. and Mishchenko, M. I.: Scattering and Radiative Properties of Morphologically Complex Carbonaceous Aerosols: A Systematic Modeling Study, Remote Sensing, 10, https://doi.org/10.3390/rs10101634, 2018.

MODIS(2022): MODIS data, available at: https://modis.gsfc.nasa.gov/data/, last access: 21 February, 2022.

Muser, L. O., Hoshyaripour, G. A., Bruckert, J., Horváth, A., Malinina, E., Wallis, S., Prata, F. J., Rozanov, A., von Savigny, C., Vogel, H., and Vogel, B.: Particle aging and aerosol–radiation interaction affect volcanic plume dispersion: evidence from the Raikoke 2019 eruption, Atmospheric Chemistry and Physics, 20, 15 015–15 036, https://doi.org/10.5194/acp-20-15015-2020, 2020.

Ohneiser, K., Ansmann, A., Baars, H., Seifert, P., Barja, B., Jimenez, C., Radenz, M., Teisseire, A., Floutsi, A., Haarig, M., Foth, A., Chudnovsky, A., Engelmann, R., Zamorano, F., Bühl, J., and Wandinger, U.: Smoke of extreme Australian bushfires observed in the stratosphere over Punta Arenas, Chile, in January 2020: optical thickness, lidar ratios, and depolarization ratios at 355 and 532 nm, Atmospheric Chemistry and Physics, 20, 8003–8015, https://doi.org/10.5194/acp-20-8003-2020, 2020.

Ohneiser, K., Ansmann, A., Chudnovsky, A., Engelmann, R., Ritter, C., Veselovskii, I., Baars, H., Gebauer, H., Griesche, H., Radenz, M., Hofer, J., Althausen, D., Dahlke, S., and Maturilli, M.: The unexpected smoke layer in the High Arctic winter stratosphere during MOSAiC 2019–2020, Atmospheric Chemistry and Physics, 21, 15 783–15 808, https://doi.org/10.5194/acp-21-15783-2021, 2021.

Ohneiser, K., Ansmann, A., Kaifler, B., Chudnovsky, A., Barja, B., Knopf, D. A., Kaifler, N., Baars, H., Seifert, P., Villanueva, D., Jimenez, C., Radenz, M., Engelmann, R., Veselovskii, I., and Zamorano, F.: Australian wildfire smoke in the stratosphere: the decay phase in 2020/21 and impact on ozone depletion, Atmospheric Chemistry and Physics Discussions, 2022, 1–41, https://doi.org/10.5194/acp-2021-1097, 2022.

Parungo, F., Kopcewicz, B., Nagamoto, C., Schnell, R., Sheridan, P., Zhu, C., and Harris, J.: Aerosol particles in the Kuwait oil fire plumes: Their morphology, size distribution, chemical composition, transport, and potential effect on climate, Journal of Geophysical Research: Atmospheres, 97, 15 867–15 882, https://doi.org/https://doi.org/10.1029/92JD01223, 1992.

Peterson, D. A., Campbell, J. R., Hyer, E. J., Fromm, M. D., Kablick, G. P., Cossuth, J. H., and DeLand, M. T.: Wildfire-driven thunderstorms cause a volcano-like stratospheric injection of smoke, npj Clim Atmos Sci, https://doi.org/https://doi.org/10.1038/s41612-018-0039-3, 2018.

Peterson, D. A., Fromm, M. D., McRae, R. H. D., Campbell, J. R., Hyer, E. J., Taha, G., Camacho, C. P., Kablick, G. P., Schmidt, C. C., and DeLand, M. T.: Australia's Black Summer pyrocumulonimbus super outbreak reveals potential for increasingly extreme stratospheric smoke events, npj Clim Atmos Sci, https://doi.org/10.1038/s41612-021-00192-9, 2021.

Polly(2022): PollyNET lidar data base, available at: http://polly.rsd.tropos.de/, last access: 21 February, 2022.

Redfern, S., Lundquist, J. K., Toon, O. B., Muñoz-Esparza, D., Bardeen, C. G., and Kosović, B.: Upper Troposphere Smoke Injection from Large Areal Fires, Journal of Geophysical Research: Atmospheres, n/a, e2020JD034 332, https://doi.org/https://doi.org/10.1029/2020JD034332, 2021.

Rieger, L. A., Randel, W. J., Bourassa, A. E., and Solomon, S.: Stratospheric Temperature and Ozone Anomalies Associated With the 2020 Australian New Year Fires, Geophysical Research Letters, 48, e2021GL095 898, https://doi.org/https://doi.org/10.1029/2021GL095898, 2021.

Rodriguez, B., Lareau, N. P., Kingsmill, D. E., and Clements, C. B.: Extreme pyroconvective updrafts during a megafire, Geophys. Res. Lett., 47, https://doi.org/10.1029/2020GL089001, 2020.

Rolph, G., Stein, A., and Stunder, B.: Real-time Environmental Applications and Display sYstem: READY, Environmental Modelling and Software, 95, 210–228, https://doi.org/https://doi.org/10.1016/j.envsoft.2017.06.025, 2017.

Rosenfeld, D., Fromm, M., Trentmann, J., Luderer, G., Andreae, M. O., and Servranckx, R.: The Chisholm firestorm: observed microstructure, precipitation and lightning activity of a pyro-cumulonimbus, Atmospheric Chemistry and Physics, 7, 645–659, https://doi.org/10.5194/acp-7-645-2007, 2007.

Rudich, Y., Sagi, A., and Rosenfeld, D.: Influence of the Kuwait oil fires plume (1991) on the microphysical development of clouds, Journal of Geophysical Research: Atmospheres, 108, https://doi.org/https://doi.org/10.1029/2003JD003472, 2003.

Shiraiwa, M., Kondo, Y., Moteki, N., Takegawa, N., Sahu, L. K., Takami, A., Hatakeyama, S., Yonemura, S., and Blake, D. R.: Radiative impact of mixing state of black carbon aerosol in Asian outflow, Journal of Geophysical Research: Atmospheres, 113, https://doi.org/https://doi.org/10.1029/2008JD010546, 2008.

Solomon, S., Dube, K., Stone, K., Yu, P., Kinnison, D., Toon, O. B., Strahan, S. E., Rosenlof, K. H., Portmann, R., Davis, S., Randel, W., Bernath, P., Boone, C., Bardeen, C. G., Bourassa, A., Zawada, D., and Degenstein, D.: On the stratospheric chemistry of midlatitude wildfire smoke, Proceedings of the National Academy of Sciences, 119, e2117325 119, https://doi.org/10.1073/pnas.2117325119, 2022.

Stein, A. F., Draxler, R. R., Rolph, G. D., Stunder, B. J. B., Cohen, M. D., and Ngan, F.: NOAA's HYSPLIT Atmospheric Transport and Dispersion Modeling System, Bulletin of the American Meteorological Society, 96, 2059 – 2077, https://doi.org/10.1175/BAMS-D-14-00110.1, 2015.

Stenchikov, G., Ukhov, A., Osipov, S., Ahmadov, R., Grell, G., Cady-Pereira, K., Mlawer, E., and Iacono, M.: How Does a Pinatubo-Size Volcanic Cloud Reach the Middle Stratosphere?, Journal of Geophysical Research: Atmospheres, 126, e2020JD033 829, https://doi.org/https://doi.org/10.1029/2020JD033829, 2021.

Stier, P., Seinfeld, J. H., Kinne, S., and Boucher, O.: Aerosol absorption and radiative forcing, Atmospheric Chemistry and Physics, 7, 5237–5261, https://doi.org/10.5194/acp-7-5237-2007, 2007.

Stocker, M., Ladstädter, F., and Steiner, A.: Observing the climate impact of large wildfires on stratospheric temperature, Nature Scientific Reports, https://doi.org/https://doi.org/10.1038/s41598-021-02335-7, 2021.

Stone, K. A., Solomon, S., Kinnison, D. E., and Mills, M. J.: On Recent Large Antarctic Ozone Holes and Ozone Recovery Metrics, Geophysical Research Letters, 48, e2021GL095 232, https://doi.org/https://doi.org/10.1029/2021GL095232, 2021.

Torres, O., Bhartia, P. K., Taha, G., Jethva, H., Das, S., Colarco, P., Krotkov, N., Omar, A., and Ahn, C.: Stratospheric Injection of Massive Smoke Plume From Canadian Boreal Fires in 2017 as Seen by DSCOVR-EPIC, CALIOP, and OMPS-LP Observations, Journal of Geophysical Research: Atmospheres, https://doi.org/https://doi.org/10.1029/2020JD032579, 2020.

Uni-Wyoming(2022): Radiosonde data, daily launches, available at: http://weather.uwyo.edu/upperair/sounding.html, last access: 21 February, 2022.

Voosen, P.: High-flying wildfire smoke poses potential threat to ozone layer, Science, 374, 921–922, https://doi.org/10.1126/science.acx9655, 2021.

Winker, D. M., Vaughan, M. A., Omar, A., Hu, Y., Powell, K. A., Liu, Z., Hunt, W. H., and Young, S. A.: Overview of the CALIPSO Mission and CALIOP Data Processing Algorithms, Journal of Atmospheric and Oceanic Technology, 26, 2310 – 2323, https://doi.org/10.1175/2009JTECHA1281.1, 2009.

Witthuhn, J., Hünerbein, A., Filipitsch, F., Wacker, S., Meilinger, S., and Deneke, H.: Aerosol properties and aerosol–radiation interactions in clear-sky conditions over Germany, Atmospheric Chemistry and Physics, 21, 14 591–14 630, https://doi.org/10.5194/acp-21-14591-2021, 2021.

Yu, P., Toon, O. B., Bardeen, C. G., Zhu, Y., Rosenlof, K. H., Portmann, R. W., Thornberry, T. D., Gao, R.-S., Davis, S. M., Wolf, E. T., de Gouw, J., Peterson, D. A., Fromm, M. D., and Robock, A.: Black carbon lofts wildfire smoke high into the stratosphere to form a persistent plume, Science, 365, 587–590, https://doi.org/10.1126/science.aax1748, 2019.

Yu, P., Davis, S. M., Toon, O. B., Portmann, R. W., Bardeen, C. G., Barnes, J. E., Telg, H., Maloney, C., and Rosenlof, K. H.: Persistent Stratospheric Warming Due to 2019–2020 Australian Wildfire Smoke, Geophysical Research Letters, 48, e2021GL092 609, https://doi.org/https://doi.org/10.1029/2021GL092609, 2021.

Table 1. Important input parameters in the self-lofting simulations, their influence on the results (in a linear or nonlinear way), and typical uncertainties in the self-lofting results caused by uncertainties in these input paramreters. More details are given in the text.

Parameter	Impact	Uncertainty
AOT	≈linear	50%
Layer thickness	≈linear	20%
Layer height	nonlinear	20%
Injection height	nonlinear	20%
BC/OC ratio	≈linear	30%
BC type	nonlinear	20%
Cloudyness	≈linear	50%
Relative humidity	nonlinear	5%
Pot. temp. gradient	linear	10%

Table 2. Main differences between stratospheric smoke layers (regarding detectable features and detectable properties) resulting from pyroCb or self-lofting processes.

	PyroCb	Self-lofting
Lofting time to tropopause	<1 h	3-7 days
Geometrical structures and pattern	spot-like plumes	blurry, homogeneous layers
Smoke particle shape	irregular	spherical
Particle depolarization ratio	≈20%	≈ 2%
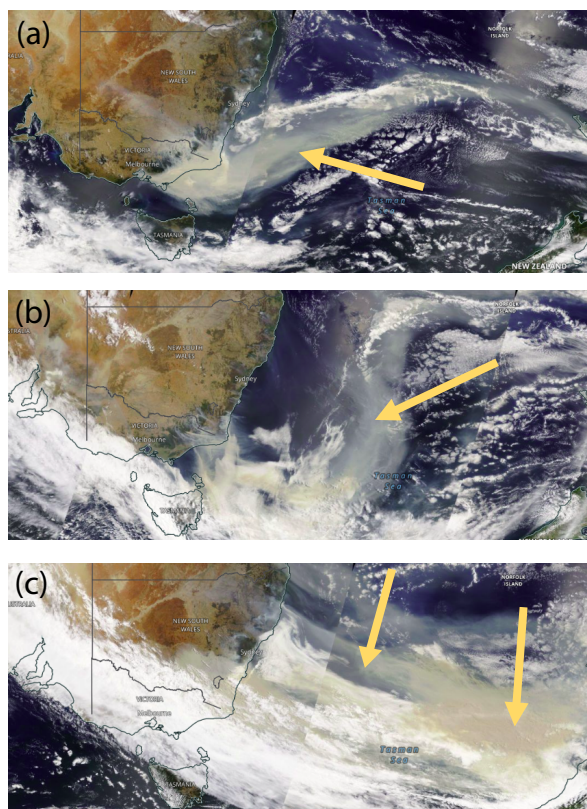
Figure 1. MODIS visible satellite images over the Pacific between Australia and New Zealand on (a) 2 January, (b) 3 January, and (c) 4 January 2020. The smoke fields indicated by yellow arrows traveled eastward towards South America.
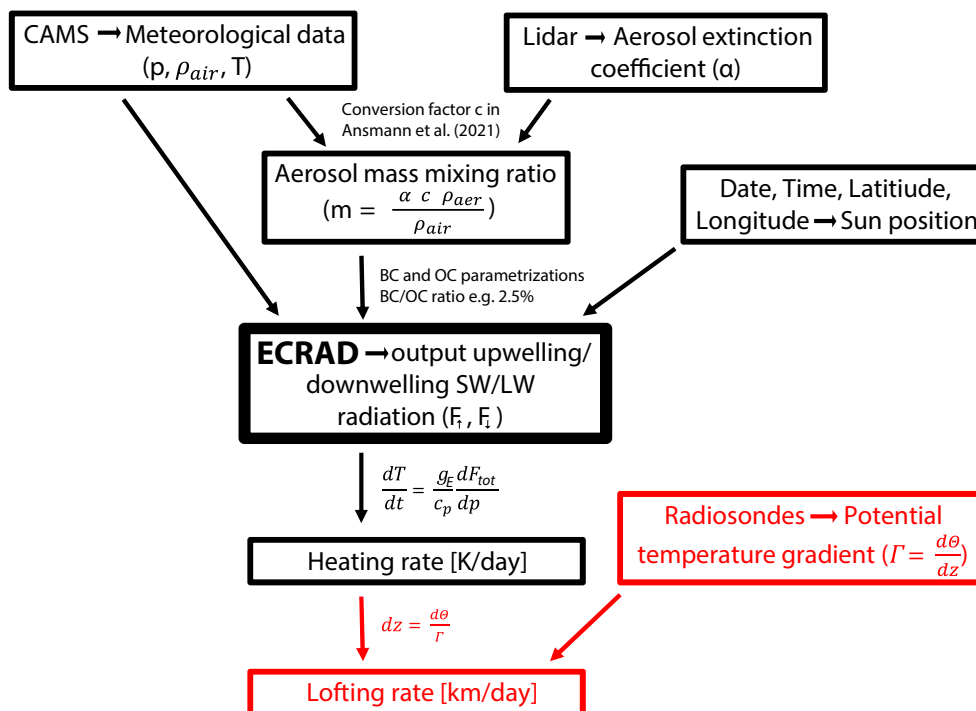
Figure 2. Simulation flowchart with the ECRAD simulation model in the center. Input are the height profile of the particle extinction coefficient (or AOT, e.g., from lidar), CAMS meteorological parameters (CAMS, 2022), and the diurnal cycle of Sun position. ECRAD output allows us to calculate heating rates. In a second, independent step (indicated in red), these heating rates, in combination with radiosonde profiles of temperature (Uni-Wyoming, 2022), are used to compute the lofting rates. Further information is given in the text.
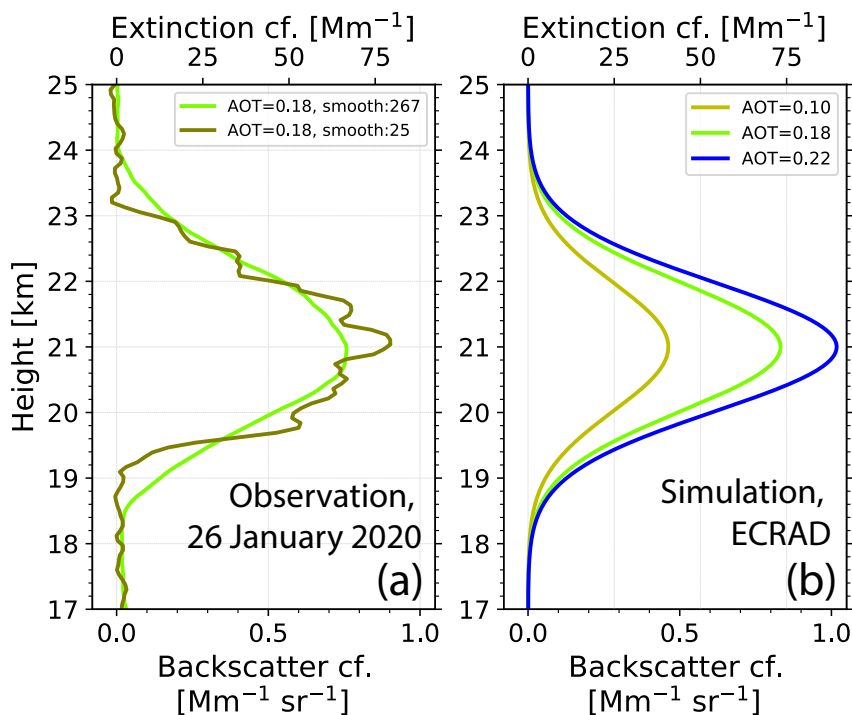
Figure 3. a) 532 nm particle backscatter coefficient of a wildfire smoke layer between 19 and 23 km height. The smoke plume was measured with ground-based lidar at Punta Arenas on 26 Jan 2020, 04:27-06:18 UTC (Ohneiser et al., 2022). The vertical signal smoothing length is 187.5 m (25 bins, olive profile) and 2002.5 m (267 bins, green profile). The extinction coefficient is obtained by multiplying the smoke backscatter coefficients with a lidar ratio of 91 sr (Ohneiser et al., 2022). The smoke layer optical thickness is 0.18. b) Parameterized backscatter and extinction profiles (Gaussian shape) with adjustable layer center and layer thickness, here for AOT=0.10, 0.18, and 0.22. The parameterized profiles are used as input in the heating rate simulations.
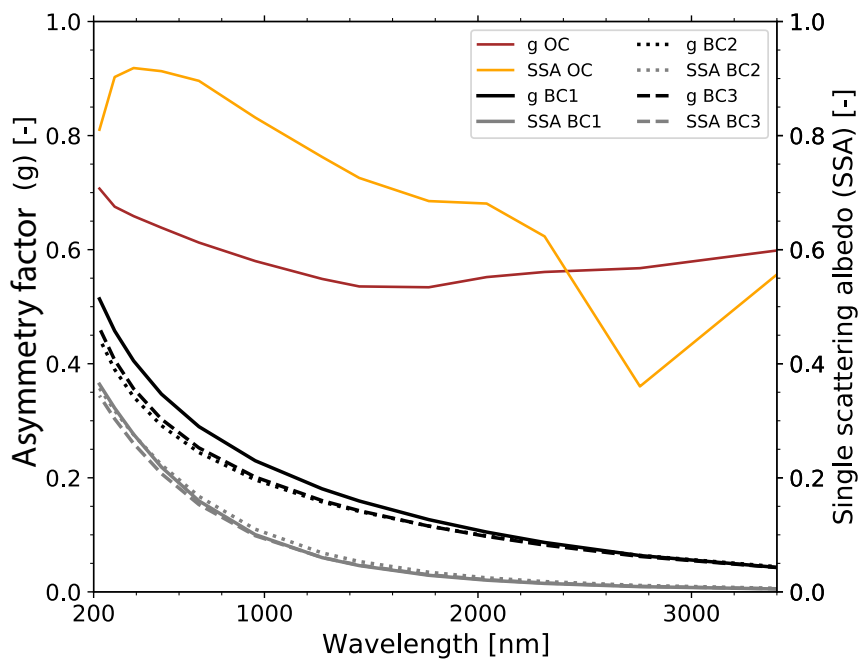
Figure 4. Optical properties of wildfire smoke. Asymmetry factor g and single scattering albedo SSA of OC (orange, brown) and for three different BC parametrizations (BC1, BC2, BC3) used in the ECRAD simulations.
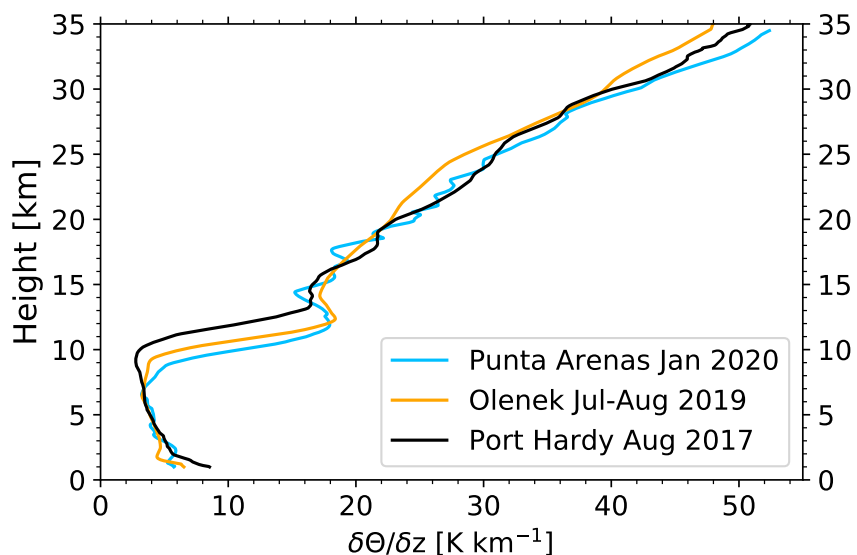
Figure 5. Gradient of the potential temperature at Punta Arenas (Chile, 53.17°S, 70.93°W, January 2020), Olenek (Russia, 68.50°N, 112.43°E, July-August 2019), and Port Hardy (Canada, 50.68°N, 127.36°W, August 2017) obtained from radiosonde data (Uni-Wyoming, 2022) and used in the self-lofting simulations (see Fig. 2).
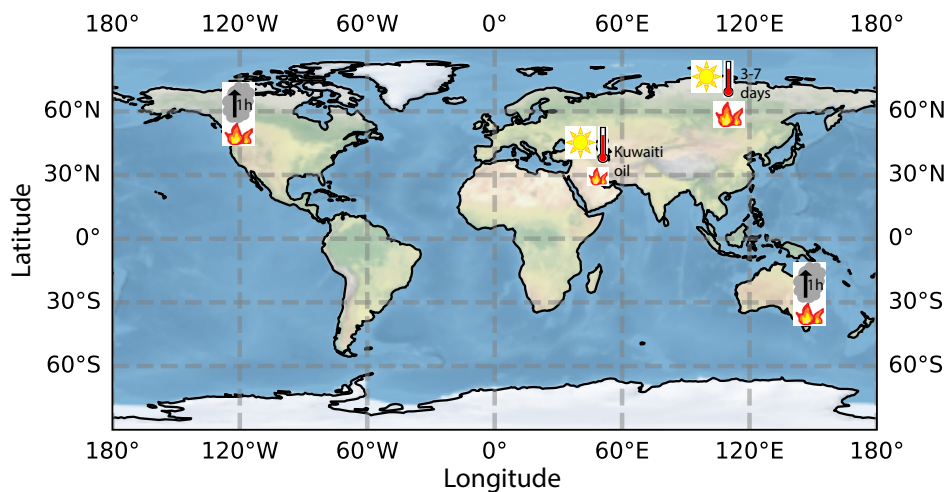
Figure 6. Map of the fire events discussed in this study. PyroCb-related smoke lofting (symbolized by a grey cloud above the fires) occurred over Britsh Columbia, Canada, in August 2017 and over Southeast Australia in December 2019 and January 2020. Self-lofting of wildfire smoke (symbolized by a sun and a thermometer over the fires) occurred over Siberia in July and August 2019 and over the oil-burning smoke areas in Kuwait, in March 1991. Smoke reaches the tropopause within a short time period (of the order of 1 h) in the case of pyroCb convection and within several days (3-7 days) in the case of self-lofting.
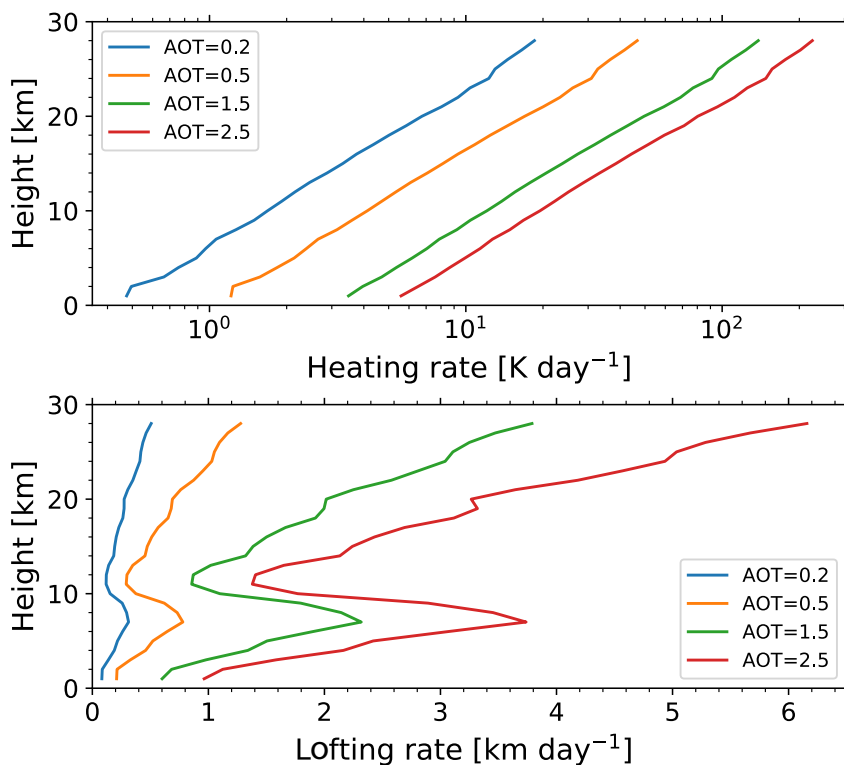
Figure 7. ECRAD simulations of (a) heating rate and (b) corresponding lofting rate as a function of height for 4 different AOTs of a 2 km thick smoke layer. The center height is stepwise increased by 1 km in the simulation from 1 km to 28 km height. The Punta Arenas temperature gradient profile in Fig. 5 is used. Daily-average heating and lofting rates are simulated.
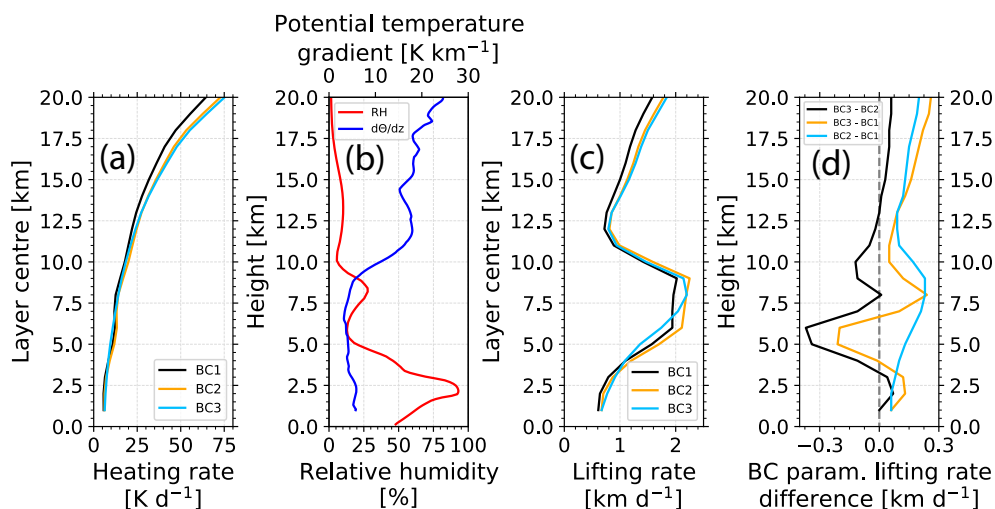
Figure 8. ECRAD self-lofting simulation (a: heating rate, c: self-lofting rate) of an ascending 2 km thick smoke layer (AOT=1.5 at 532 nm, Punta Arenas, 26 January 2020) for three different BC parametrizations shown in Fig. 4. The relative humidity in (b) influences the BC parametrization. In (d), differences between lofting rate solutions by considering two of the three BC parametrizations (BC1, BC2, BC3) are shown. The simulated daily-average heating and lofting rates are given for the layer center height.
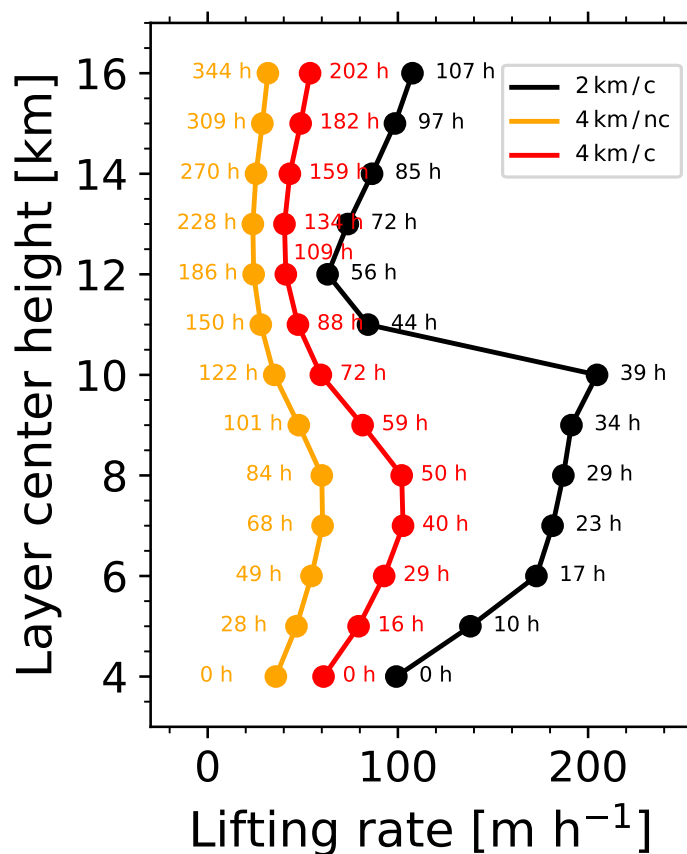
Figure 9. Simulation of self-lofting of a wildfire smoke layer. The 532 nm AOT of the 2-km (black profile) and 4 km (orange and red profiles) thick smoke layers, initially centered at 4 km height, was assumed to be 2.0. Two overcast ('c' - cloudy, black, red) scenarios and one clear sky ('nc' - no clouds, orange) scenario are simulated. Numbers indicate the time in hours after start of lofting.
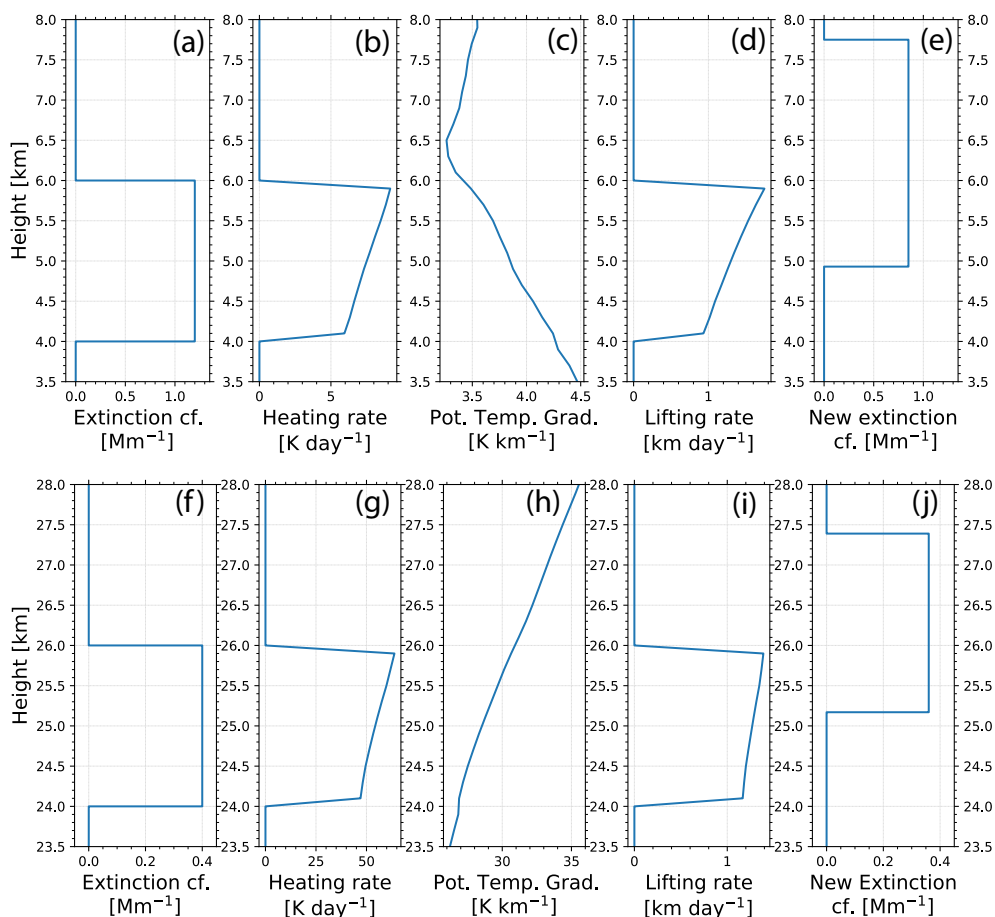
Figure 10. Self-lofting effects on layer depth in the troposphere (a-e, layer at 4-6 km height before lofting) and in the stratosphere (f-j, layer at 24-26 km height before lofting). Step by step calculation of the new layer profile after 1 day of heating and lofting. The extinction profiles in (a) and (f) were used in the simulations, (b) and (g) show the resulting heating rate profiles, (c) and (h) the potential temperature profiles at Punta Arenas assumed in the simulations, (d) and (i) the resulting lofting rate profiles, (e) and (j) finally the resulting new extinction coefficient profiles in the troposphere and stratosphere after 1 day of self-lofting.
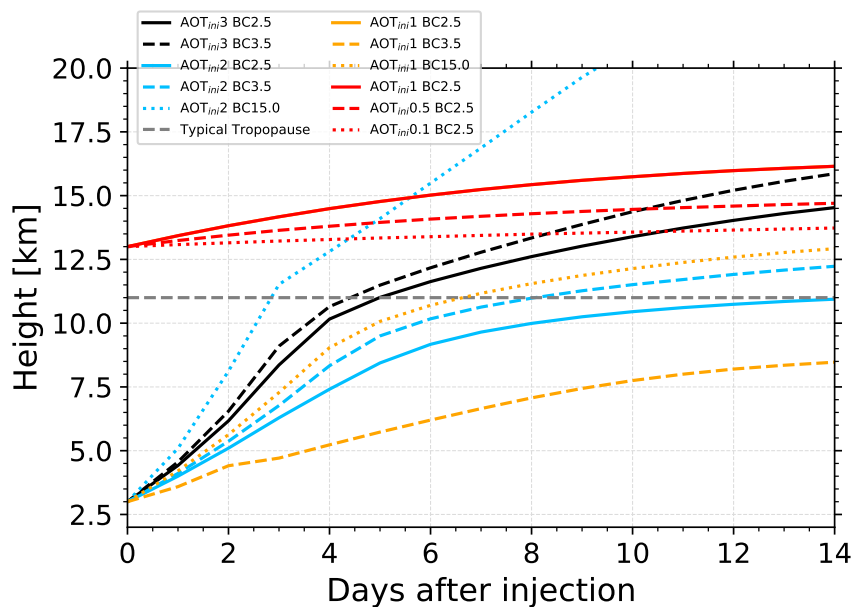
Figure 11. Change of the center height of a 2.5 km thick aerosol layer, initially at 3 km height (day 0), during 14 days of continuous lofting (black, blue, orange). In the simulation, the AOT continuously decreases by 15% from day to day. Different scenarios with different initial AOT of 1, 2, and 3, and BC fraction of 2.5%, 3.5% and 15% are simulated. In addition, the lofting behavior of a stratospheric layer initially at 13 km height (red lines, see legend regarding AOT and BC fraction, 15% AOT decrease from day to day) is shown. The grey dashed line represents a typical tropopause height in the mid-latitudes.
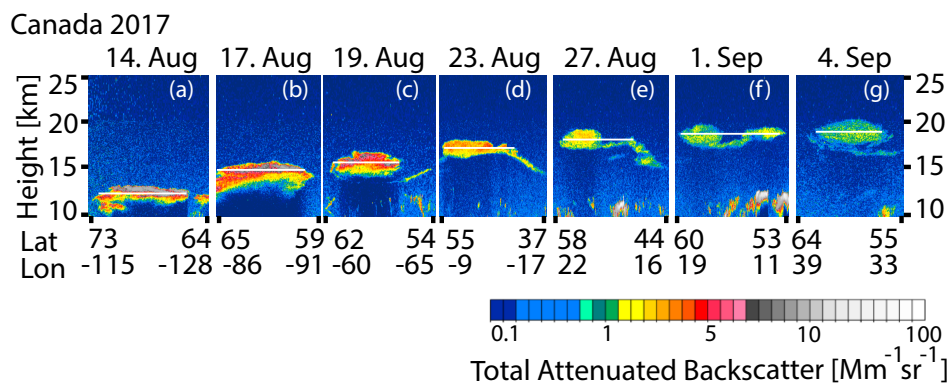
Figure 12. Height-time display of the total 532 nm (Rayleigh + particle) attenuated backscatter coefficient of a Canadian wildfire smoke layer observed with CALIOP on 6 different days within the three-week period from 14 August to 4 September 2017. The white horizontal lines indicate the layer center height of the ascending smoke layer.
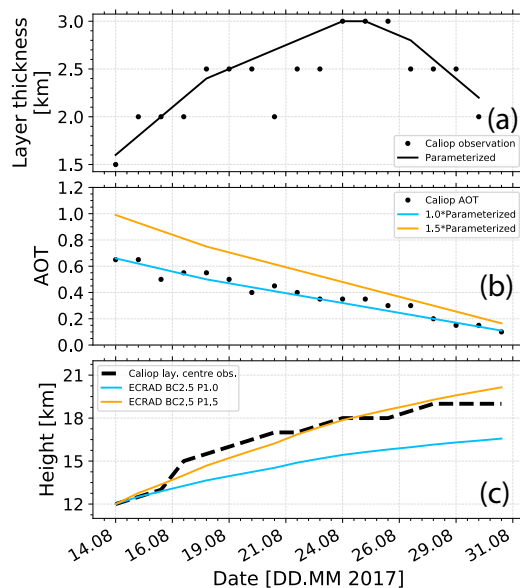
Figure 13. Comparison of CALIOP observations with respective ECRAD simulations of the self-lofting behavior of a Canadian smoke plume observed at 12 km height on 15 August 2017, 00:00 UTC (in panel c). In (a), the layer thickness obtained from the CALIOP observations in Fig. 12 is shown and parameterized. In (b), the AOT observations are given. The CALIOP layer mean total attenuated backscatter coefficient was multiplied with a lidar ratio of 65 sr (Baars et al., 2019) and with the layer thickness in (a) in order to retrieve the daily AOT (black dots). Two parameterized time series of AOT (blue, based on the estimated AOT values, P1.0, 1.0 times the observed CALIOP AOT) and a second one (orange, estimated AOT·1.5, P1.5, parametrization 1.5 times the CALIOP observation) were used in the simulations. By using these parameterizations (solid curves) in (a) and (b), the heating rates and subsequent lofting rates are simulated, shown in (c) and compared with the observed lofting rates (black dashed line).
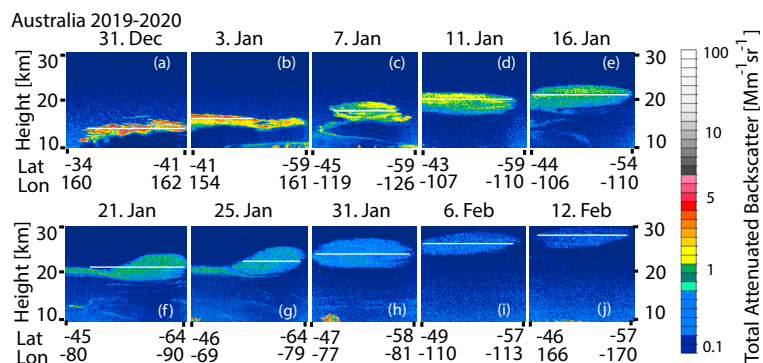
Figure 14. Height-time display of the total 532 nm attenuated backscatter coefficient of an Australian wildfire smoke layer observed with CALIOP on 10 different days within the 6.5-week period from 31 December 2019 to 12 February 2020. The white horizontal lines indicate the layer center height of the ascending smoke layer.
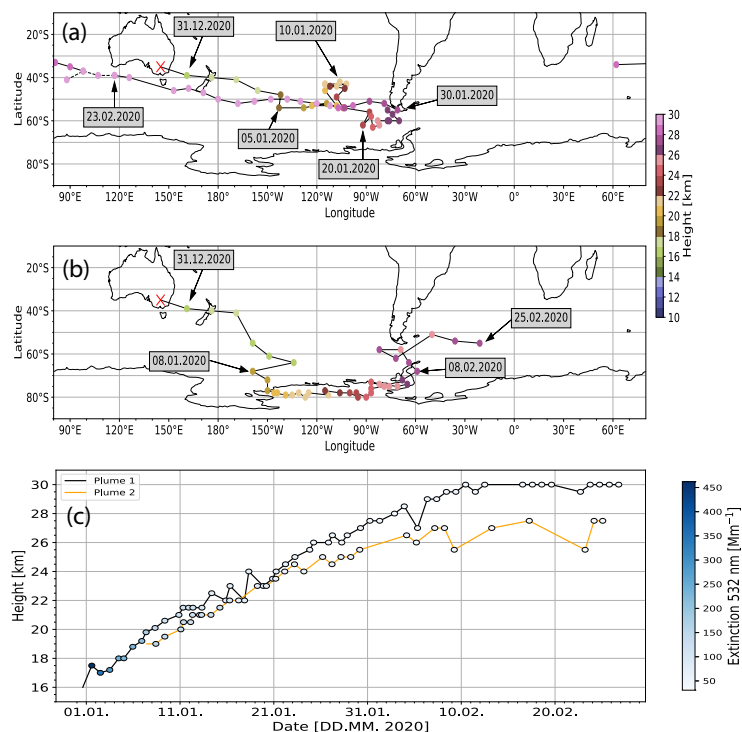
Figure 15. Geographical location and altitude of two main Australian fire smoke plumes during their travel in January-February 2020. In (a), the position of the smoke layer 1 (Plume 1) is shown. The color of the dots indicates the height of the smoke layer center (see legend on the right). In (b), the travel of the smoke layer 2 (Plume 2) is shown. In (c), the ascent behavior of the two different layers in January and February 2020 is presented.
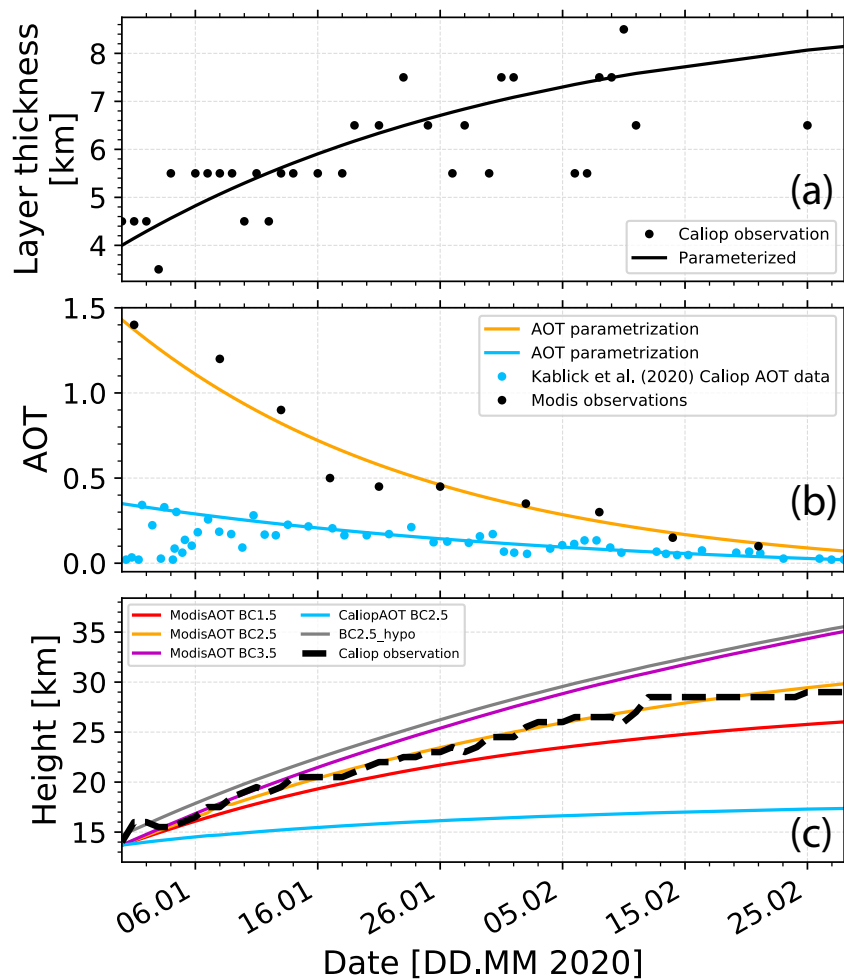
Figure 16. Comparison of CALIOP observations with respective ECRAD simulations of the self-lofting behavior of an Australian smoke plume observed at 14 km height on 31 December 2019 (in panel c). In (a), the layer thickness obtained from the CALIOP observations in Fig. 14 is shown and parameterized. In (b), the AOT observations are given, retrieved from the CALIOP observations (blue dots, (Kablick et al., 2020)) and independently also from MODIS observations (black dots). By using the parameterizations (solid curves) in (a) and (b), the heating rates and subsequent lofting rates are simulated, shown in (c) and compared with the observed lofting rates (black dashed line). Different BC fractions of 1.5%, 2.5%, and 3.5% for the MODIS AOT parameterizations (red, orange, magenta, respectively) and for 2.5% for the CALIOP AOT parameterization (blue) are considered as well. In addition, the simulation shown in grey (BC_hypo) assumes an injection at 15 km height instead of 14 km and a BC fraction of 2.5%.
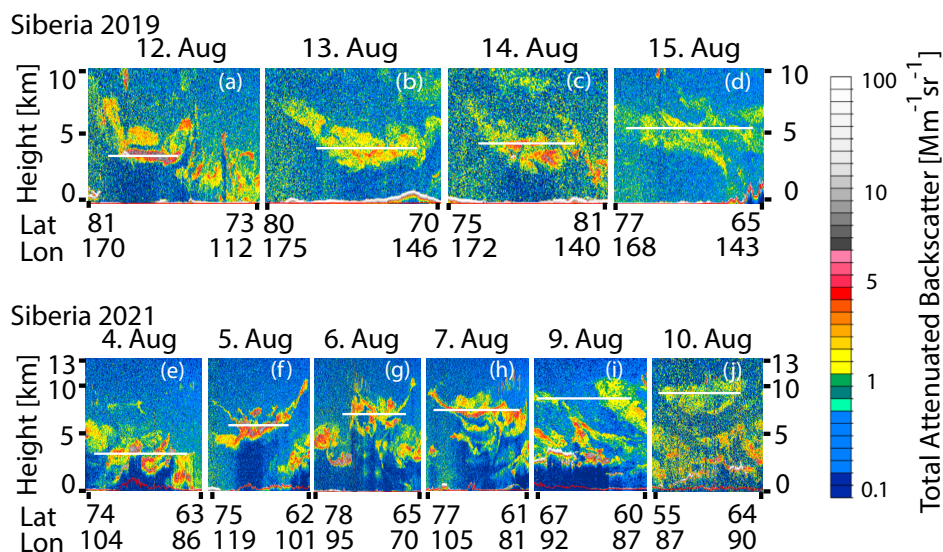
Figure 17. Height-time display of the total 532 nm attenuated backscatter coefficient of Siberian wildfire smoke plumes observed on (a) 4 days in August 2019 and (b) 6 days in August 2021. The white horizontal lines indicate the layer center height of an ascending smoke structure.
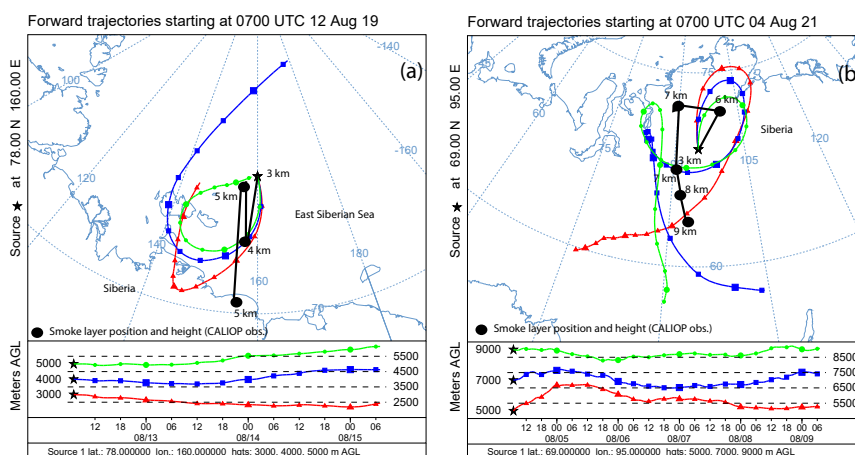
Figure 18. HYSPLIT (Hybrid Single-Particle Lagrangian Integrated Trajectory) 3-day forward trajectories (Stein et al., 2015; Rolph et al., 2017) for (a) 12 August 2019, 7:00 UTC, starting at 3 km (red), 5 km (blue) and 7 km height (green) above the ground footprint of the CALIOP lidar beam and (b) 4 August 2021, 7:00 UTC, starting at 5 km (red), 7 km (blue) and 9 km height (green) above the CALIOP position (HYSPLIT, 2022). The black dots indicate the position of the smoke layer center each 24 h as observed with CALIOP and shown in Fig. 17, the numbers indicate the height of the layer centre.
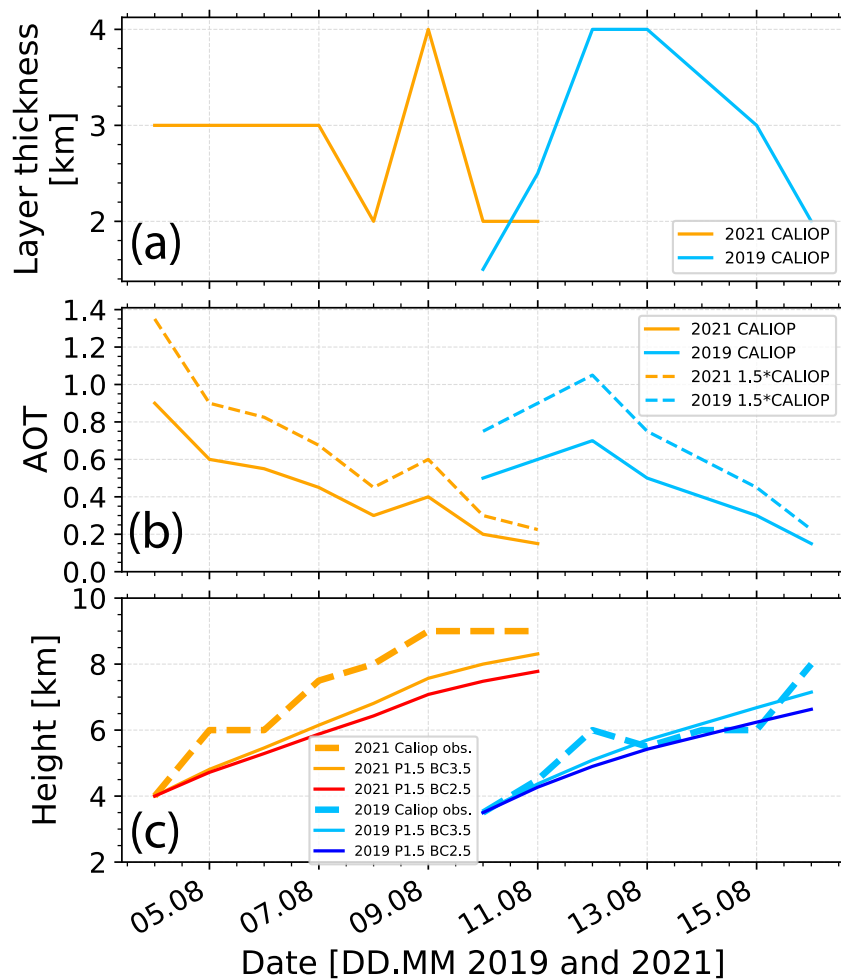
Figure 19. Comparison of CALIOP observations with respective ECRAD simulations of the self-lofting behavior of tropospheric Siberian smoke in August 2019 (in blue in panel c) and in August 2021 (in orange in panel c). In (a), the layer thickness obtained from the CALIOP observations in Fig. 17 is shown and parameterized. In (b), the AOT observations are given, retrieved from the CALIOP observations. Two parameterized time series of AOT (blue, based on the estimated AOT values, P1.0 meaning parametrization with 1.0 times the observed CALIOP AOT) and a second one (orange, estimated AOT·1.5, P1.5, the observed CALIOP AOT times 1.5) were used in the simulations in (c). By using these parameterizations in (a) and (b), the heating rates and subsequent lofting rates are simulated, shown in (c) and compared with the observed lofting rates (dashed lines). Different BC fractions of 2.5%, and 3.5% are considered as well.